Geochemical and petrographic investigation of Triassic and Late Miocene organic-rich intervals from onshore Cyprus, Eastern Mediterranean

Sebastian Grohmann, Maria-Fernanda Romero-Sarmiento, Fadi Henri Nader, François Baudin, Ralf Littke

Geochemical and petrographic investigation of Triassic and Late Miocene organic-rich intervals from onshore Cyprus, Eastern Mediterranean

Sebastian Grohmann*[,1,2,3], Maria-Fernanda Romero-Sarmiento[2], Fadi Henri Nader[2], François Baudin[3] and Ralf Littke[1]

* Corresponding author: sebastian.grohmann@emr.rwth-aachen.de

[1] Energy & Mineral Resources Group (EMR), Institute of Geology and Geochemistry of Petroleum and Coal, RWTH Aachen University, Lochnerstrasse 4-20, 52056 Aachen, Germany

[2] IFP Énergies nouvelles (IFPEN), Direction Géosciences, 1 et 4 Avenue de Bois-Préau, 92852 Rueil-Malmaison Cedex, France

[3] Institut des Sciences de la Terre de Paris, Sorbonne Université, CNRS, 4 place Jussieu, 75005 Paris, France

Abstract

In order to improve the understanding of potential petroleum systems in the still underexplored Eastern Mediterranean Sea, two field campaigns were performed to investigate potential source rocks onshore Cyprus. Elemental data (total organic (TOC) and inorganic carbon (TIC), total sulfur (TS), Fe, Ni, V), Rock-Eval® pyrolysis, biomarker and microscopic analysis (organic petrography, random vitrinite reflectance (VR_r), palynofacies) of the obtained Mesozoic to Cenozoic samples have proven the existence of organic matter (OM) rich deposits within the following two geological formations:

(1) The Triassic Vlambouros Formation (Fm.) of the Mamonia Complex comprises frequently occurring, few centimeter thin clay layers interbedded between meter thick sandstone units. The clay layers of this formation are characterized by TOC contents of about 1 wt.% representing a Type III kerogen showing hydrogen index (HI) values of 48 mg HC/g TOC on average. VR_r values of 0.5 to 0.6 % as well as several biomarker ratios indicate low thermal

maturity. The formation was deposited at the northern margin of Gondwana and similar strata may be present in the basement of the Levant Basin and the Eratosthenes Seamount. There, thermal maturity would be higher and such rocks might contribute to thermogenic gas systems.

(2) In the Miocene Pakhna Fm., OM-bearing intervals are mainly present in the upper part of the formation in outcrops east of the Troodos Mountain, while organic-rich intervals are very scarce to absent in the south and southwest of the island. The eastern outcrops show abundant fine-grained, (marly) mud- to wackestones interbedded between coarser-grained carbonates. The fine-grained intervals have TOC contents of about 4 wt.% representing mainly Type II-III kerogen with HI values of 238 mg HC/g TOC on average. The OM is immature as indicated by VR_r values between 0.3 and 0.5 %. TS/TOC ≥ 2.8 and several biomarker ratios indicate oxygen-depleted, even anoxic conditions during deposition. A negative correlation between the TOC and TIC indicates that such conditions were reached during enhanced primary bioproductivity controlled by local and regional clastic derived nutrient input. Similar conditions may have been present along the southeastern margin of the Eratosthenes Seamount, south of Cyprus. Presence of abundant organic matter and high sedimentation rates during the Miocene were favorable for microbial gas generation in the deeper parts of the basins.

Keywords

Eastern Mediterranean, Cyprus, source rocks, organic geochemistry, organic petrography

1. Introduction

During the last decade, several large gas field discoveries were made in the offshore Levant and Herodotus basins (Fig. 1A), in the Eastern Mediterranean Sea (Ratner, 2016, Cyprus Mail, 2018). These new fields comprise mainly natural gas of biogenic origin and are located in either Miocene clastic turbidites (e.g. Tamar & Leviathan (Israel), Aphrodite (Cyprus); Montadert et al., 2014; Bou Daher et al., 2016) or in Mesozoic shallow marine carbonates (Zohr (Egypt), Calypso (Cyprus); Bertello et al., 2016, Esestime et al., 2016). Especially the latter ones set up a new kind of play target for the whole area. A very new gas discovery of 5 to 5 trillion cubic feet of gas (Tcfg) was recently confirmed offshore Cyprus in block 10 (ExxonMobil, 2019).

For petroleum system assessments (either thermogenic or biogenic) and the reduction of exploration risks, qualitative as well as quantitative information about the spatial distribution of potential petroleum source rocks is required in order to predict both the type and amount of generated HC. In the Eastern Mediterranean offshore region, the characterization of potential source rocks is not a simple task, since almost no public well data and core samples are available. Therefore, source rock properties and distribution have to be deduced from seismic interpretation and nearby onshore observations. Accordingly, a lot of work has been done for the southern and eastern margins of the Levant Basin (e.g. Abed et al., 2005; El Nady, 2007; Hawie et al., 2013a; Bou Daher et al., 2014; Bou Daher et al., 2015; Ghalayini et al., 2018). Recently Grohmann et al. (2018) showed the existence of potential source rock intervals on the Eratosthenes Seamount (ESM) offshore southern Cyprus. Nevertheless, the western and northern margins of the Levant Basin remain relatively underexplored.

In this context, we present here a review of potential petroleum source rocks in the Eastern Mediterranean Sea and enhance the current, available data base with new geochemical and petrographic results obtained from Triassic and Late Miocene organic-rich rocks from the onshore area of Cyprus. In this study, two consecutive field campaigns were carried out in 2016 and 2017 to collect potential source rock intervals from onshore Cyprus. These rocks

were investigated with respect to both the quantity and quality of sedimentary organic matter (OM), their source rock potential, thermal maturity, and the corresponding depositional environment. All this information is used to discuss the possible mechanisms of source rock deposition and petroleum systems in the greater area of Cyprus.

2. Geological setting

The evolution of the Eastern Mediterranean Sea began in Late Paleozoic time and is until today mainly determined by the interplay of the African, Arabian and Eurasian plates (Fig. 1A). During the Pangaea breakup, the area was located at the northern margin of Gondwana (Robertson et al., 2012). Several, mainly northwest-southeast oriented rifting phases in Jurassic and Triassic time caused the disintegration of Gondwana and the evolution of the Neo-Tethys Ocean (Segev and Rybakov, 2010; Hawie et al., 2013a; Ghalayini et al., 2014). During these rifting phases, the Herodotus and the Levant Basin were formed and separated by the Eratosthenes Continental Block (ECB) (Montadert et al., 2014). Based on vector magnetic anomaly data, the Herodotus Basin is interpreted to be floored with oceanic crust (e.g. Makris and Stobbe, 1984; Granot, 2016), whereas there are different hypothesis for the crustal style of the Levant Basin: Gardosh and Druckman (2006) proposed an oceanic crust, whereas recent studies have indicated that the basin's basement is made up by thin (~8 km), stretched continental crust (Granot, 2016; Inati et al., 2016, Inati et al., 2018). Between these two basins, the ECB presents a long-lasting bathymetric high. In its center, the ESM (Fig. 1A and B), a huge, up to 6 km thick, isolated carbonate platform evolved (Montadert et al., 2014; Papadimitriou et al., 2018). The basins, however, comprise thick sedimentary fills of 14-16 km in the Herodotus Basin and 12-14 km in the Levant Basin (Montadert et al., 2014).

During the Late Cretaceous, the tectonic regime changed from an extensional setting to a compressional one. Afro-Arabia started to move northwards and a north-verging subduction zone evolved along the southern margin of Eurasia (Hawie et al., 2013a; Montadert et al., 2014). In the Turonian, between 90 and 92 Ma, slab-pull related extension along the southern Eurasian margin caused the formation of new oceanic crust above the subduction

zone (Regelous et al., 2014). Consecutively, in the Maastrichtian (~70 Ma) parts of this new oceanic crust were obducted onto the northern Afro-Arabian margin (Garfunkel, 2004). One of these ophiolitic complexes is the Troodos Ophiolite, today representing the basement of the island of Cyprus (Henson et al., 1949; Swarbrick and Robertson, 1980; Lord et al., 2000). At the time of initial obduction, Cyprus was still in a deep marine setting (2000-3000 m water depth) far away from any continental margins. This is well illustrated by white chalk and chert deposits of the Late Cretaceous to Early Miocene Lefkara Formation (Fm.) (Fig. 1B and 2) (Kähler, 1994; Kähler and Stow, 1998; Lord et al., 2000).

In the Oligocene, the evolution of an active hot spot caused the breakup of Afro-Arabia with an accelerated northward drift of the Arabian plate. Consequently, the Levant Margin experienced strong uplift, causing erosion and the incision of canyons along the margin and high input of clastic material into the Levant Basin (Gardosh et al., 2008; Nader, 2014). Since the Mid Eocene, the shrinking Neo-Tethyan Ocean became continuously separated from the Indian Ocean in the east with the final isolation of the Eastern Mediterranean Sea in the Early-Middle Miocene (Robertson et al., 2012). During the Latest Miocene, the Mediterranean Basin was also cut off from the Atlantic Ocean resulting in the Messinian Salinity Crisis (MSC) (Hsü et al., 1977; Krijgsman et al., 2002; Meilijson et al., 2018). Throughout almost the entire Mediterranean Basin, thick sequences of salt (up to 2 km) were deposited while the ESM was exposed above sea-level and subjected to meteoric water flushing (Robertson, 1998), before the whole area was re-flooded again in the Pliocene (Hsü et al, 1977; Krijgsman et al., 2002).

Since the Early Miocene, the ESM is in a state of collision with the Troodos Ophiolite along the Cyprus Arc (Fig. 1). This has caused a strong uplift of the area, especially until the mid-late Pleistocene, leading to the rise of Cyprus above sea level (Robertson, 1998; Galindo-Zaldivar et al., 2001, Kinnaird et al., 2011). During the Miocene, this ongoing convergence, in combination with transpressional forces related to the faster movement of the Arabian plate, caused the formation of several, separately tectonically controlled sub-basins, that can be observed around the rising Troodos Mountain (Fig. 1B) and throughout the offshore area

along the Cyprus Arc (Reiche et al., 2016; Symeou et al., 2018). These sub-basins were partly restricted from the open sea (Eaton and Robertson, 1993). The sedimentation during this period is represented by the carbonate deposits of the Pakhna Fm. (Fig. 1B and 2), which is divided into the lower Terra Member (shallow water bioclastic carbonates) and the Upper Koronia Member (coral reef carbonates) (Eaton and Robertson, 1993; Lord, 2000). The different tectonic regimes led to varying accumulated thicknesses. While the formation's thickness spans approximately 250 m in the Polemi Basin in the west (Fig.1B and 2), it reaches up to 400 m in the Khalassa Basin in the south and in the Mesaoria Basin in central Cyprus, respectively (Kinnaird et al., 2011). At the end of the Miocene, most of the shallow water environments around the Troodos Mountain were also affected by the MSC, which is indicated by the gypsum deposits of the Kalavasos Fm. (Fig.2) (Krijgsman et al., 2002).

3. Petroleum source rocks in the Eastern Mediterranean

Whether OM accumulates and is preserved in the sedimentary pile or not depends on several factors such as (a) elevated primary bioproduction of OM, (b) enhanced preservation due to anoxic bottom waters, (c) burial rate, which determines for how long the OM is subjected to oxidation if anoxic bottom waters are not present, as well as (d) specific decomposition kinetics depending on the type of OM (Bohacs et al., 2005; Katz, 2012). Often it is an interplay between these factors that control the formation and quality of petroleum source rocks. Throughout the geological history of the Eastern Mediterranean Sea, several periods provided conditions that favored the deposition and preservation of OM (e.g. high oxygen depletion due to strong upwelling in the Late Cretaceous (e.g. Bou Daher et al., 2015) or very high sedimentation rates during the Oligo-Miocene (e.g. Nader, 2014)) and led to the formation of major regional petroleum source rocks.

During the syn-rift phase in the Early to Middle Mesozoic, extension related subsidence led to the flooding of the area. With ongoing subsidence, first shallow water carbonate platforms evolved, which later evolved into deep marine carbonate environments (Barrier and Vrielynck, 2008). In this setting, organic-rich rocks are believed to have been deposited along

the passive continental margin. In northern Egypt, Mid-Jurassic source rocks are thought to be present deeply buried below the Nile Delta and to be responsible for thermogenic generation of oil and gas (Wigger et al., 1997; Shaaban et al., 2006). Also in the area of Lebanon, Triassic to Mid-Jurassic OM-rich limestones are considered as potential source rock intervals (Ghalayini et al., 2018). In Israel, thermogenic hydrocarbons (HC) are present in Jurassic and Cretaceous reservoirs, although no specific source could be assigned (Feinstein et al., 2002).

With the change to a compressional regime at the end of the Mesozoic, the whole region was located in a slope to basinal clastic marine environment, with the exception of the ECB and the Troodos Ophiolite, on which deep marine carbonate platforms began to evolve (Barrier and Vrielynck. 2008; Papadimitirou et al., 2018). During the Late-Cretaceous to Early-Cenozoic, a large-scale upwelling system affected the southern shallow epicontinental shelf of the Tethyan Ocean (Levant margin) providing cold and nutrient-rich waters (Almogi-Labin et al., 1993). Consequently, increased bio-productivity led to the formation of extensive source rock intervals, reported as fine grained limestones of Turonian to Lower Maastrichtian age with total organic carbon (TOC) contents up to 11 wt.% in Lebanon (Bou Daher et al., 2014; Bou Daher et al., 2015) or phosphatic oil shales and bituminous limestones of Late Maastrichtian to Paleocene age with TOC contents up to 22 wt.% in Jordan (Abed et al., 2005). These source rocks comprise mainly Type II or Type II-S kerogen and are of low thermal maturity in the onshore area. Bou Daher et al. (2015) observed that TOC contents decrease towards the deeper parts of the Levant Basin. Nevertheless, with the assumption that source rocks are still present in the deeper basin, Bou Daher at al. (2016) demonstrated that the oil-window thermal maturity is reached in the offshore area and thermogenic HC generation is likely to have occurred between 34 and 16 Ma in Upper Cretaceous source rocks.

The separation of the African and the Arabian plates (see above) in the Oligocene-Miocene caused a major uplift of the Levant area leading to an increased influx of sediments derived from the Nile Delta as well as from the Levant margin (Inati et al., 2018). As a result, the

environment changed from a carbonate to a more siliciclastic-dominated setting at the Early/Late Oligocene boundary (Buchbinder et al., 2005). For this period, organic-rich intervals have developed in the Nile Delta in the Oligocene to Miocene (Shaaban et al.,2006), which may be responsible for natural gas and condensate accumulations(Wigger et al., 1997). Also at the southeastern Levant margin, offshore Israel, the geochemical analysis of different oil and gas samples indicates different sources of biogenic gas. Corresponding source rocks might be located in the Eocene, Oligo-Miocene, and Plio-Pleistocene (Feinstein et al., 2002). Furthermore, Bou Daher et al. (2016) and Schneider et al. (2016) suggested that Oligo-Miocene source rocks potentially present in the offshore area of Lebanon are likely to have produced biogenic gas, similar to the gas that is present in the Tamar and Leviathan fields offshore Israel.

From Late Mesozoic until Mid-Cenozoic, the area of Cyprus was located far away from any continental margins and, thus, exposed to different depositional conditions compared to the Levant Margin (Barrier and Vrielynck, 2008). In the southern offshore area of Cyprus, Grohmann et al. (2018) investigated Late Cretaceous to Messinian intervals along the ESM. The studied sections comprise mainly argillaceous carbonates to pure limestones with low organic contents (average TOC around 0.2 wt.%). More clay-rich sections with increased amounts of Type II kerogen (TOC contents up to 5 wt.%) and, in general, good hydrocarbon generation potentials are present in the lower Upper-Cretaceous (Turonian to Coniacian) and Upper Eocene (Bartonian to Priabonian) intervals. While the older source rock intervals are likely be restricted to the closer surrounding of the ESM, organic-rich post-Mid-Eocene units might extend also in the deeper parts of the Levant Basin.

Onshore Cyprus, evidence for the existence of organic-rich intervals is reported for the Paleogene Lefkara Fm. (Kähler and Stow, 1998) and within the Miocene Pakhna Fm. (Eaton and Robertson, 1993). Furthermore, bituminous sandstones are observed in Triassic and Jurassic formations within the Mamonia Complex (Lapierre, 1975; Robertson and Woodcock, 1979). However, previous studies are based on rock descriptions without any modern geochemical investigations. Therefore, the main objective of this work isto investigate these

formations in greater detail by means of geochemical and petrographic analysis to better identify and characterize the potential source rock intervals throughout the onshore Cyprus region, and to better understand their implications for offshore HC exploration.

4. Samples and methods

4.1. *Sampling representative outcrop rocks: Onshore Cyprus*

A total of 147 samples, which were suspected to be enriched in OM (chosen mainly by fine grain size and dark color), were collected from the onshore area of Cyprus. Samples were taken from at least 30 cm below the outcrop surface in order to reduce the risk of major weathering effects. Figure 1B shows a simplified geological map of the island. Sample locations are widespread throughout the southern island (Fig. 1B, Table 1).

In the Mamonia Complex (a mélange of autochthonous rocks that were over-thrusted onto the Troodos Ophiolite during the Late Cretaceous; Lapierre, 1975; Robertson and Woodcock, 1979), samples originate from both the Triassic Vlambouros and the Jurassic Episkopi formations. The Vlambouros samples originate from thin shaly clay intervals which are interbedded with thick sandstone successions at Location (Loc.) 31 and 32 (Fig. 1B and 3). Large (> 1mm) plant remains can be recognized in both, the clay-rich as well as in the sandstone units. Similar organic-rich clay layers can be observed at Loc. 24 (Fig. 1B), where they are interbedded with massive calcarenites. All three outcrops are likely to be part of a passive continental margin, fluvio-deltaic environment. Loc. 31 and 32 represent a more clastic, proximal setting while Loc. 24 should represent a more distal calcareous system. The Episkopi samples are mainly dark, reddish-deep brown claystones, which are referred to deep marine slump deposits.

In the Circum Troodos Sedimentary Succession (autochthonous sediments around the Troodos Ophiolite) samples are described according to Dunham (1962) although some of the samples contain elevated amounts of fine grained argillaceous material. Samples were collected from the Late Cretaceous-Paleocene Lefkara Fm. comprising greyish mudstones, and from the Miocene Pakhna Fm. In the Khalassa (Loc. 20 and 21) and Maroni (Loc. 11 and

12) basins (Fig. 1B), the collected Pakhna samples are representative of a few, thin dark brown mudstone layers, which are interbedded with massive limestones. More towards the northeast, in the Cyprus (Loc. 10) and Mesaoria (Loc. 1) Basins, instead, two thick successions of greyish black mud- to wackestones relatively regularly interlayered between wacke- to grainstones were sampled in greater detail (Fig. 4).

4.2. Sample preparation

Prior to the organic geochemical and microscopic investigations, all samples were dried over night at 50°C. Ground rock powder was prepared from large representative rock pieces using a disc mil to ensure homogeneity of the samples.

Total organic matter (TOM) concentrates were prepared for the more organic-rich samples (based on TOC results, see next section) of the Vlambouros and Pakhna Fm. for further detailed analysis. Approximately 10 g of sample were crushed to a grain size of 1-2 mm using a quartz mortar, in order to avoid destruction of organic particles. TOM isolation was performed following the standard non-oxidizing acid treatment and drying procedures described by Durand and Nicaise (1980). The crushed material was placed in plastic beakers and treated with 150 ml of HCl (35%) to destroy carbonate minerals. After the reaction ceased, boiling water was added to enable the destruction of dolomite. When all particles settled down, the water was removed and the beaker refilled with fresh deionized water. For subsequent silicate removal, the samples were treated with 150 ml of HF (75%) for 15 hours, followed by two washes with deionized water. 150 ml of boiling HCl (35 %) were used to decompose any minerals formed during the HF attack, such as fluorosilicates. At the end, the organic residue was washed with 80°C hot, distilled water until a neutral pH value was reached. Samples were centrifuged (3500 rotations/min) to settle all the organic matter and allow the water to be decanted. One part of the sample material was kept in water for later preparation of glass slides for microscopic palynofacies analysis. The other part was dried in an oven at 50°C to evaporate the remaining water.

4.3 Elemental analysis

4.3.1 Bulk rock (TOC, TIC, TS, Fe, Ni, V)

For quantification of the carbon content, a *LiquiTOC II* device equipped with a module for solid analysis (*Elementar*) was used. Total organic (TOC) and inorganic carbon (TIC) contents were determined directly by measuring the amount of CO_2 evolving from 100 mg of powdered sample during combustion at 550 and 1000°C, respectively, by an IR detector (detection limit 10 ppm, TOC error 0.6%, TIC error 1.7%).

Total sulfur (TS) content was determined for all bulk rock samples using a *LECO S-200* instrument. 100 mg of powdered rock sample were combusted in a ceramic crucible at 1800°C. Oxygen was used as carrier gas and for sulfur oxidation to SO_2, which was measured by an IR detector (detection limit 20 ppm, error < 5%).

In addition, the iron (Fe), nickel (Ni) and vanadium (V) contents were measured for 37 bulk rock samples with significant TS contents via X-ray fluorescence. Measurements were performed on thick, homogenized pellets of 8 g pulverized (<63 µm) bulk rock mixed with 2 g of a *Fluxene CEREOX* wax using a *SPECTRO XEPOS ED(P)-RFA* instrument (detection limit ≤ 1.4 ppm; error for Ni and V < 2%, error for Fe < 0.2%).

4.3.2. Total organic matter concentrates(C, H, N, TS, O)

Carbon (C), hydrogen (H), nitrogen (N), and total sulfur (TS) concentrations were determined on ten TOM concentrates using a *FLASH 2000 Organic Elementar Analyzer* by *ThermoFischer SCIENTIFIC*. Aliquots of 1 to 2 mg were placed in soft tin crucibles together with a small amount of vanadium pentoxide (V_2O_5), acting as a catalyst. Combustion was performed at 1600 °C resulting in the formation of CO_2, H_2O, SO_2, SO_3, and NO_x. The latter two molecules were reduced to SO_2 and N_2 and remaining O_2 was fixed to copper. The generated molecules are transported by a helium flux, separated by gas chromatography and detected by thermal conduction detector (TCD) with a lower detection limit of < 0.5 µg and an accuracy of ± 0.2%.

The oxygen (O) content was determined using the same device. Sample material was capped in small, soft silver crucibles without adding any catalyst. Instead of combustion, the sample was pyrolyzed at 1065 °C under a helium atmosphere. Pyrolysis products are N_2, H_2, CH_4, and CO (representing the oxygen contained in the sample), which were again separated by gas chromatography and detected by the TCD with a lower limit of ≤ 1 µg and an accuracy of ± 0.2%.

4.4 Rock-Eval pyrolysis

In order to evaluate the source rock potential of the analyzed rocks, Rock-Eval® analysis (Espitalié et al., 1977) was performed using a *Rock-Eval® 6 Complete Analysis – Serial Process* device (*Vinci Technologies*). The *IFP Basic/Bulk-Rock Method for Source Rocks* was used for 50 mg of powdered sample following the procedures described in Behar et al. (2001). The sample was heated under a nitrogen atmosphere at isothermal 300°C for 3 min with consecutive temperature increase by 25°C/min up to 650°C. In this study, the Hydrogen (HI) and Oxygen Index (OI) were determined from the Rock-Eval® S2 and S3 peaks in relation to the TOC content determined by the elemental analyzer.

Additionally, ten TOM concentrates (5 mg) of the Pakhna Fm. were analyzed using the *IFP Pure Organic Matter Method* also described in Behar et al. (2001), following the same heating program but reaching a final pyrolysis temperature of 800°C. It is assumed that all generated CO and CO_2 are in this case of organic origin.

4.5 ***Biomarker analysis***

15 samples were selected for molecular geochemical analysis to represent each outcrop. For outcrops with numerous samples low and high TOC samples were chosen. Maltene extracts were first obtained by accelerated solvent extraction (ASE) using a *DIONEX ASE 150* instrument (*ThermoFischer SCIENTIFIC*), which allows a full automatic extraction. Approximately 4 g of pulverized bulk rock sample were extracted by 40 ml of dichloromethane (DCM) in a high pressure cell at 100°C and 100 bar during 14 min. The

maltene extracts were separated into three fractions by means of silica-gel based liquid chromatography and eluents of different polarity: 5 ml of pentane to obtain the aliphatic fraction, 5 ml pentane/DCM (40:60) for the aromatic fraction, and 5 ml methanol for the polar fraction. Only the first fraction was selected for further analysis, due to the low thermal maturity of the samples.

4.5.1 *GC-FID*

For the relative determination of *n*-alkanes as well as the *iso*prenoids pristane (Pr) and phytane (Ph), a *Carlo Erba Strumentazione HRGC 5300* gas chromatograph equipped with a flame ionization detector (GC-FID) was used. The starting temperature was set to 60 °C and kept for 3 min. Afterwards, the temperature was increased by 5 °C/min up to 310 °C and held for 20 min. 1 µl of concentrated sample was injected in splitless mode set to 60 s. Compound separation was achieved using a 30 m long *Zebron ZB-1* capillary column and hydrogen as carrier gas. The obtained chromatograms were interpreted using the *Atlas CDS* software.

4.5.2 *GC-MS*

For the analysis of hopanes and steranes gas chromatography coupled with mass spectrometry (GC-MS) was performed using a *Mega Series HRGC 5160* gas chromatograph (*Carlo Erba, IT*) equipped with a 30 m x 0.25 mm x 0.25 µm film *Zebron ZB-5_MS* fused silica capillary column. For specific detection a quadrupol mass spectrometer Trace MS (*Thermoquest*) was used. 1 µl of sample was injected by split injection at 80°C. After 3 min isothermal hold, temperature was first increased by 10°C/min up to 160°C, followed by a further temperature increase by 3°C/min up to 320°C, which was held for 20 min. Helium was used as carrier gas with a velocity of 30 cm/s. Hydrocarbons were analyzed in single ion mode (EI+, 70 eV, measured m/z = 58, 85, 191, 205, 217, 218, 259, 372, 386, 400, 412) with a source temperature of 200°C.

Hopanes and steranes were evaluated based on m/z = 191 and m/z = 217, respectively. The identification of different compounds is based on a CHIRON reference standard

(Hopane/Sterane Calibration Mix) and by comparison with other reference material. For peak quantification the *Xcalibur* software (*ThermoFinnigan*) was used.

4.6 Organic petrography and palynofacies analysis

Organic petrography was performed on 21 samples covering the most organic rich samples (> 1wt.% TOC, where possible) from all investigated outcrops. Polished sections were prepared by embedding bulk rock pieces of approximately 2 cm x 2 cm in a two compound epoxy resin and consecutively polishing perpendicular to their bedding planes. For maceral analysis, a Zeiss Axio Imager.M2m microscope equipped with a 50x/1.0 Epiplan-NEOFLUAR Oil Pol objective and PI 10x/23 ocular lens was used. Maceral identification was based primarily on their difference in reflectivity as well as their fluorescence intensity under ultra-violet light following procedures described by Taylor et al. (1998). Random vitrinite reflectance (VR_r) was measured using a Zeiss Axioplan microscope equipped with a 50x/1.0 EC-Epiplan-NEOFLUAR Oil Pol objective lense and a PI 10x/23 ocular lenses. Calibration was performed using a Leuco-Saphir standard with a reflectance of 0.592%. VRr values were calculated as the mean of at least 50 measured single vitrinite grains. More details of the preparation and microscopic analysis are described in Sachse et al. (2011).

Additionally, 10 OM-rich samples (TOC > 1 wt.%) originating from Loc. 10 were investigated with respect to their pyrite framboid size distribution. According to Wilkins et al. (1996), approximately 100 individual framboid diameters were measured in randomly chosen parts of the polished sections in order to produce statistically relevant distributions. For each distribution, the mean diameter, the standard deviation, and the skewness of the distribution were calculated.

Twenty-one TOM concentrates were chosen for palynofacies analysis according to the same criteria as for organic petrography, representing the same outcrops and similar facies as for the organic petrography. Due to the limited availability of sample material, not always exactly the same samples were chosen. The analysis was performed following procedures described in Tyson (1995). Aliquots of the TOM were sieved (> 10 µm) and mounted on glass slides for

the microscopical analysis. The quantitative determination of the palynological compounds was based on the sieved kerogen fraction larger than 10 µm. Counting was performed under normal transmitted light using a 40x magnification objective and an ocular with a 10x10 grid to determine the relative areal abundance of the different components.

5. Results and interpretation

5.1 Organic matter-richness and carbonate content

The TOC content is widely used as an indicator of the quantity of OM in sedimentary rocks (Peters, 1986). A minimum of 0.3 wt.% TOC is required for (calcareous) sediments to be considered potential source rocks (Hunt, 1967). 60 of the 147 investigated samples exceed this threshold (Table 2) and will be discussed in the following. These samples are assigned to the Triassic Vlambouros Fm. and the Miocene (mainly Upper) Pakhna Fm.

The organic-rich samples of the Vlambouros Fm. are characterized by average TOC contents of around 1 wt.%, with one exception (sample 262) that shows a TOC content of 7 wt.%. The TIC contents in these samples are very low with 0.02 wt.% on average at Loc. 31 and 32 (Fig. 1B and Fig. 3) and higher at Loc. 24 with an average of 2.7 wt.% (Fig. 1B).

Carbon contents of the Pakhna samples vary between the different locations with 0.3 to 6.7 wt.% TOC and 0.7 to 8.7 wt.% TIC. The higher TOC contents are observed at the northeastern outcrops at Loc. 1 and 10 (Fig. 4) with 4.4 wt.% on average, while the southwestern outcrops (Fig. 1B) show average values of 1.6 wt.%.

In the TOM concentrates of the Pakhna samples, the TOC contents vary between 31 and 57 wt.%. A TOC content of about 70 wt.% is to be expected for immature marine kerogen (Stock et al., 2017). Thus, the organic matter content ranges from about 71 to 81 % for the Pakhna TOM concentrates with the exception of one sample (44 %) proving that these are relatively clean total organic matter plus pyrite concentrates.

5.2 Source rock quality and thermal maturity

Based on the Rock-Eval® results (Table 2), the Vlambouros samples are characterized as terrestrial, gas-prone Type III kerogen in the pseudo- van Krevelen diagram (Fig. 5A) with HI values between 18 and 73 mg HC/g TOC and OI values between 21 and 150 mg CO_2/g TOC. The Pakhna samples plot somewhere between the marine, oil/gas prone Type II to and Type III kerogen pathways (Fig. 5A), with HI values ranging from 21 to 384 mg HC/g TOC and OI values ranging from 35 to 319 mg CO_2/g TOC.

It is known that the Pakhna Fm. was deposited in a marine environment (e.g. Eaton and Robertson, 1993). Although it is not uncommon to find terrigenous organic matter/type III kerogen in marine settings, some of the OI values seem to be exceptionally high while some of the HI values seems to be too low for OM deposited in a marine setting. In the HI vs. T_{max} diagram (Fig. 5B) the samples plot closer towards Type II kerogen, but still some of the samples tend towards Type III. These results can be explained as follows:

1) Samples originating from outcrops are affected by weathering and potentially oxidation of the OM, which would lead to increased OI and T_{max} values (Littke, 1993).
2) During pyrolysis, some unstable, immature carbonates could decompose at low temperatures. Also, organic acids can be generated during pyrolysis, which dissolve parts of the carbonate. Both produce additional CO_2, which would cause an overestimation of the OI (Katz, 1983). This case has been observed previously for organic-rich carbonates along the ESM, offshore Cyprus (Grohmann et al., 2018).
3) For samples with low TOC contents, HC generated during pyrolysis can be retained to different extents depending on the type and amount of clay minerals contained in the mineral matrix, leading to a decrease of the recorded S2 peak and, therefore, to a reduced HI value (Espitalié et al., 1984).

In the present case, the first effect is considered to be of less importance, since the microscopic investigation of the samples show mainly fresh pyrite (Fig. 6A and C), which is usually more vulnerable to weathering than OM (Littke, 1993). Only one sample with intensely weathered pyrite could be observed (Fig. 6G and H).

To investigate the other two possible effects, Rock-Eval® results obtained from 11 representative bulk rocks samples of the Pakhna Fm. were compared with their corresponding TOM concentrates (Table 3). Figure 7A and B illustrate the Rock-Eval® pyrograms for the bulk rock and TOM aliquots of one high (Fig. 7A) and one low TOC (Fig. 7B) sample normalized by the TOC content and the sample weight. It can be seen that a high proportion of thermovaporized and pyrolyzable HC is retained by the mineral matrix. The effect is stronger in the sample with the lower bulk TOC content (Fig. 7B). This effect causes higher HI values for the TOM concentrates (Table 3). At the same time, the OI values are lower (Table 3). Both, the increase in the HI and the decrease in the OI seem to be more pronounced if the bulk rock samples have low TOC contents (Fig. 7C). As a result of both effects, the TOM concentrates plot closer to the kerogen Type II pathway than the respective bulk rock samples (Fig. 7D) and are in accordance with the classical kerogen classification based on the H/C vs. O/C atomic ratios (Fig. 7E). Although Rock-Eval® analysis for bulk rock samples is a standard technique in petroleum exploration, the HC generation potential might be severely underestimated, especially for samples with low-moderate TOC content if measured on bulk rock.

Thermal maturity of sedimentary OM is another crucial parameter for the characterization of source rocks since their hydrocarbon generation potential changes with thermal maturation and the related loss of functional groups (e.g. Peters et al., 2005; Zieger et al., 2018). Thermally, the Vlambouros samples are marginally mature as indicated by Rock-Eval® T_{max} values between 434 and 442°C and VR_r values of 0.51 to 0.63% (Table 2 and 4; Fig. 8A). The Pakhna samples are thermally immature as indicated by T_{max} values between 424 and 428°C and VR_r values of 0.33 to 0.48% (Table 2 and 4; Fig. 8A). The very low thermal maturity in both formations is further supported by the predominance of odd-numbered *n*-alkanes (Fig. 9A) expressed by a carbon preference index (CPI) or odd-even predominance (OEP) mostly > 1 (Table 5) as well as by the preference of 20R- and αββ-configuration of the analyzed steranes (Fig. 8B, Table 6) (Bray and Evans, 1961; Peters et al., 2007).

All analyzed parameters indicate thermal immaturity of the Pakhna samples. Thus, it can be assumed that the results represent the initial quality of the OM. The samples of the Vlambouros Fm. are marginal mature, so that the initial HC generation potential might have been slightly higher. Nevertheless, the HC generation potential of the Vlambouros samples is very low and the organic-rich intervals are only a few centimeters thick (Fig. 3). Therefore, this formation cannot be considered as a typical petroleum source rock.

The Pakhna samples, instead, especially the northeastern successions at Loc. 1 and 10 are of very good quality according to the classification by Peters et al. (2005). Furthermore, the actual HC potential might be even higher, due to the observed mineral matrix effect. However, it should be noted that the total observable thickness for this formation at the outcrop scale ranges between 10 to 20 meters, which is at the lower limit for high-quality source rocks.

5.3 Origin of organic matter and paleo-redox conditions

Petrographic (Fig. 6 I and J) and palynological observations (Fig. 10D and 11) show that the OM in the Vlambouros Fm. is almost exclusively composed of large (25 to > 50 µm) terrestrial particles. This is in accordance with the Rock-Eval® results (Fig. 5). Most of the woody particles are characterized as highly oxidized palynomacerals (PM) of Type 4 and 1 (Fig. 10D and Fig. 11) pointing towards a deposition under oxygenated conditions (Tyson, 1995).

The Pakhna samples are characterized by a fine-grained siliciclastic and/or calcareous matrix (Fig. 6A and C) showing yellow-brownish fluorescence under ultra-violet light excitation (Fig. 6B and D). This “organic” fluorescence has been observed in other marine, OM-rich sediments, in particular from upwelling areas, and attributed to the presence of submicroscopic (< 1 µm) hydrogen-rich (liptinitic/sapropelic) groundmass (Littke and Sachsenhofer, 1994) or “fluoramorphinite” (Senftle et al., 1987). In addition, larger liptinites like alginites are relatively abundant, which are oriented parallel to the bedding (Fig. 6D and F). Terrestrial macerals like vitrinites and inertinites are less common in all Pakhna samples.

Their lowest abundance is observed in samples from outcrops with only thin and less organic-rich intervals (mainly in the southwest) (Fig. 6E).

Pyrite occurs mainly as epigenetic pore filling crystals in foraminifera in the samples from the outcrops with thinner and less organic-rich intervals (mainly in the southwest) (Fig. 6G and H). In the samples of the thicker and more organic-rich intervals (Loc. 1 and 10, northeast) instead, syngenetic pyrite framboids are highly abundant (Fig. 6A and C).These framboids show mean diameters of 3 to 4.2 µm with a generally skewed distribution towards larger diameters (Fig. 12A). This may serve as an indicator that crystal growth took place in the water column, as it is the case under anoxic bottom water conditions (Fig. 12B and C; Wilkins et al., 1996, 1967). However, clearly larger frambiods of >5 up to 26 µm can also rarely be observed (Fig. 12A). Such big framboids usually form only in the anoxic pore waters within the sediment underlying oxygenated water columns (Willkins et al. 1996, 1967). Hence, the here investigated samples are interpreted to represent paleo-redox conditions varying from dysoxic to anoxic.

In general, both OM as well as framboidal pyrite in the Pakhna samples are more abundant in the more siliciclastic parts of the rocks and less common in the more calcareous intervals. This observation can also be made at the outcrop scale, where the OM- and clay-rich intervals are interbedded with OM-lean and more calcareous intervals. Hence, the original sediment composition before bacterial sulfate reduction was estimated according to Littke (1993) (Fig. 13, see figure caption for detailed description). For the Pakhna samples, the amount of OM seems to increase with increasing silicate and decreasing carbonate content. There are two possible interpretations for this relationship: On the one hand, it may indicate that nutrient supply and thus bioproductivity were positively affected by the deposition of siliciclastic material (Ricken, 1993), leading to higher accumulation of OM in the sediment. On the other hand, in case oxygenated bottom waters were still present, increased clastic sedimentation, especially of argillaceous material, would increase the burial efficiency by insulating the OM and shifting the oxic-anoxic boundary within the sediment closer towards the sediment-water interface. This would as well increase the potential of OM preservation.

Further parameters useful for the interpretation of paleo-redox conditions can be obtained from the abundance of TS, Fe, Ni, and V. Their concentrations are shown in Table 7. Bacterial sulfate reduction is controlled by the availability of OM. Thus, under normal marine conditions, formation of pyrite results in a positive correlation between TOC and TS values, with ratios varying around 2.5 (Berner, 1984). This is also the case for many of the Pakhna samples from southwestern Cyprus (Fig. 14A). Oxygen depletion in the bottom water promotes bacterial sulfate reduction already in the water and leads to TOC/TS ratios lower than 2.5, as it can be observed for many Pakhna samples from eastern Cyprus (Fig. 13A). Sulfate-depleted and oxygenated environments result in significantly larger TOC/TS ratios, as observed for most of the Vlambouros samples (Fig. 14A). This is consistent with the assumed fluvio-deltaic environment for this formation, where a distinct influence of freshwater can be expected leading to low sulfate concentrations

Another redox indicator is the ratio V/(V + Ni) which, however, should be always combined with other results, as the V/(V+Ni) ratio usually points more towards reducing conditions compared to other parameters (Szczepanik et al., 2007). Nevertheless, for the Pakhna samples, these ratios are quite high (Fig. 14B) representing Eh conditions that are only reached under conditions of enhanced bacterial sulfate reduction (Lewan, 1984). To verify whether the measured TS originates from pyrite and is not to a major percentage of organic origin, TS and Fe contents were compared (Dean and Arthur, 1989). For the analyzed set of samples, TS/Fe ratios smaller than 1.15 indicate that sulfur is mainly present in the form of iron sulfide, in agreement with other interpretations (Fig. 14C). Thus, elemental data indicate dys- to anoxic conditions for the Pakhna samples and mainly oxic conditions for the Vlambouros samples.

Another set of data are specific biomarker ratios which are useful to interpret the origin of OM and the redox conditions during deposition (Tables 5 and 6, Figs. 15 and 16). The ratio of Ph/*n*-C_{18} vs Pr/*n*-C_{17} (Fig. 15 A and B) confirms a mainly terrestrial type of OM deposited under oxic conditions for the Vlambouros samples. In contrast, C_{27}-steranes (Fig. 15C and

16) indicate for two samples also a contribution of marine OM, which, however seems reasonable, as a deltaic environment is assumed for this formation.

Biomarker ratios indicate a marine to mixed type of OM for most Pakhna samples and the redox conditions are interpreted as oxygen depleted (Fig. 15 A, B, C). The ratio of C_{27}-, C_{28}-, and C_{29} regular steranes confirms a marine environment (Fig. 16). Furthermore, very low (<1) Gammacerane Index values disagree with high salinity, i.e. there was no high salinity event before the Messinian salinity crisis. Tricyclic hopanes C_{22}/C_{21} vs. C_{24}/C_{23} (Fig. 15 D) indicate carbonate-dominated to siliciclastic marine conditions, in accordance with lithological and petrological observations.

6. General discussion and hypotheses on the offshore area

The integrated geochemical and petrographic analysis of 147 Mesozoic to Cenozoic outcrop samples from onshore Cyprus prove the existence of organic-rich intervals in the Triassic Vlambouros Fm. as well as in the Miocene Pakhna Fm.

Samples of the Vlambouros Fm. comprise early mature gas-prone Type III kerogen, which was deposited under oxic conditions. These samples are mainly representative of thin, clay-rich layers interbedded with massive sandstone packages. However, even in some of the sandstones, terrestrial organic particles could be proven, leading to elevated concentrations of TOC in these intervals.

Samples of the Pakhna Fm. reveal immature, medium to high quality, marine, oil- and gas-prone Type II kerogen. However, biomarker analysis shows that also subordinate terrestrial material is present. The following sections present a first depositional concept for the larger area, which could explain why the Miocene organic-rich deposits are present east of the Troodos Mountain and almost absent in the southern parts of the island.

6.1 Mechanisms of source rock deposition (Pakhna Fm.)

The distribution of OM within the Pakhna Fm. is proposed to be the result of (1) the tectonic setting combined with (2) paleo-climatic, and (3) local and regional paleo-geographic conditions during the Late Miocene:

1) The collision of the ESM with the Troodos Ophiolite during the Miocene caused the formation of several small piggy-back basins along the Cyprus Arc. Simultaneously, the Cyprus area experienced a strong uplift, with the strongest uplift occurring in the southern-central part of the island (Symeou et al., 2018).
2) Climatic conditions during the Late Miocene, with mainly west to east oriented ocean and wind currents, were comparable to those that can be observed today in the Mediterranean region (Kouwenhoven and van der Zwaan, 2006; Rohling et al., 2015). However, during the Late Miocene (already before the MSC), the sea level was significantly lower than today (Haq et al., 1988). Under this low sea level, the uprising island of Cyprus, the ESM, as well as the large Nile Cone Delta might have acted as barriers protecting the easternmost part of the Eastern Mediterranean Sea from high energy water currents. A consequence would have been calmer water bodies, where less mixing took place enhancing the chance of oxygen depletion.
3) Bioproductivity largely depends on the availability of nutrients (Nixon et al., 1986), which are usually derived from terrestrial sources of clastic material (Van der Zwaan and Jorissen, 1991). Related to the paleo-geographic and topographic setting during the Late Miocene, the input of nutrients into the Mesaoria and Cyprus basins is likely to have been significantly higher than into basins located south of the Troodos Mountain. While the local terrestrial supply towards the Khalassa and Maroni basins was restricted to the Troodos source area, the Mesaoria and Cyprus basins were also fed by the already emerged Kyrenia Range in the north. More regional sources for terrestrial input at that time were the Nile Cone Delta in the south, the uprising Levant Margin in the east (Nader, 2014), and probably also the Latakia region at the northeastern edge of the Levant Basin (Hawie et al., 2017). Favored by the isolated, calm-water environment, plumes of fine sediments and nutrients might have

propagated over long distances towards the (south-) eastern rim of the barrier. Therefore, local as well as regional nutrient supply would have favored an increased bio-productivity in basins east of the Troodos.

Thus, an increased bio-productivity together with calm waters might have led to oxygen depletion and the formation of dysoxic (to probably even anoxic) bottom waters and finally to the deposition and preservation of OM-rich intervals as they are described here for the eastern Pakhna outcrops. Furthermore, in the case of still oxygenated bottom waters, the increased clastic sedimentation rates would have also favored the preservation of OM.

6.2 Implications on petroleum systems in the Eastern Mediterranean Sea

Due to the general lack of publicly available well data in the Eastern Mediterranean Sea, any extrapolation from on- to offshore areas, especially in the Cyprus Arc region, is hard to accomplish. However, some assumptions can be made as follows:

Lapierre et al. (2007) suggest that the Late Triassic sediments of the Mamonia Complex represent remnants of the old northern passive continental margin of Gondwana. Hence, these sediments would correlate with those underlying the ESM in the southern offshore area of Cyprus, as well as the Levant Basin in general. Triassic rocks under the ESM are buried by 6 km of overlying strata and they are interpreted to be at depths of around 11 km in the deepest part of the Levant Basin (e.g. Montadert et al., 2014; Bou Daher et al., 2016). At such depths, similar gas-prone Type III kerogen bearing clay- and sandstone intervals like those observed in the Vlambouros Fm. might have produced thermogenic gas enriched in ethane, which was announced to be present in the recently discovered Calypso 1-field in Cyprus offshore block 6 (CyprusMail, 2018).

During the Late Miocene, increased bio-productivity and preservation of OM seem to have been restricted to the basins east of the Troodos Mountain, since almost no OM-rich deposited can be found in the southern area. This scenario is in accordance with the observations made by Grohmann et al. (2018), who could not prove any OM-bearing intervals within Miocene sections along the central and northern ESM. Respecting the above-

explained local and regional factors (barrier effect of Troodos and ESM, calm water conditions, long distance transport of fine sediments and nutrients from Nile and northern Levant area), it can be assumed that similar constellations allowed the deposition of source rocks also at the northern and western margins of the Levant Basin. These locations, in particular, might be the southern flank of the Hecateus Rise and Latakia Ridge, as well as the southern and eastern flank of the ESM (Fig. 1). Hence, OM production would be mainly increased in front of these barriers. TOC contents might be similar to those observed onshore eastern Cyprus, but are expected to gradually decrease towards the deeper parts of the basin, depending on the extend of the created oxygen minimum zone.

Middle to Late Miocene clastic sediments, derived either from the Nile Cone Delta or from the Levant Margin, are described as fan and turbidite deposits reaching far into the northern Levant Basin (Hawie et al., 2013b). Their distal, sandy lobes are stacked over each other and are intercalated with more clay- (Hawie et al., 2013b; Hawie et al. 2017) and probably organic-rich deposits. Furthermore, numerical simulations performed by Schneider et al. (2016) have shown that sedimentation rates, especially in the Middle and Upper Miocene, were favorable for biogenic gas generation almost throughout the whole deeper parts of the basin. With these assumptions, the Middle – Late Miocene successions would represent self-charging reservoirs, which are sealed by the Messinian salt.

For future perspective works, all geochemical results and the proposed conceptual depositional models presented here, can be tested and used by extending previous numerical depositional models (Hawie et al., 2017) towards the western margin of the Levant Basin. This will allow a better prediction of the lateral extent of potential source rocks in the Eastern Mediterranean Sea. Such source rock models in combination with biogenic as well as thermogenic petroleum system modeling (such as Schneider et al., 2016; Bou Daher et al., 2016) can provide an integrated approach, which can help to better understand and predict HC generation and accumulation in this underexplored frontier area.

7 Conclusion

The geochemical and microscopic investigation of a great number of Mesozoic to Cenozoic samples prove the existence of organic-rich deposits onshore Cyprus. Such intervals were found within (1) the Triassic Vlambouros Fm. and (2) the Miocene Pakhna Fm. and can help do get a better idea of potential source rocks at the northwestern margin of the Levant Basin:

(1) Respective intervals in the Vlambouros Fm. are composed of thin clay layers, containing about 1 wt.% TOC in the form of terrigenous, gas-prone Type III kerogen. The OM shows early thermal maturity. The formation represents an extended depositional system formed at the northern continental margin of Gondwana, which is also to be expected in the basement of the ESM and the Levant Basin. There, similar gas-prone intervals might contribute to thermogenic gas, which was announced to be present in the Calyso 1 field, offshore Cyprus.

(2) Promising source rock intervals in the Pakhna Fm. are restricted to the upper part of the formation and were only observed east of the Troodos Mountain. Frequently occurring mud- to wackestone layers show TOC contents of about 4 wt.%. Rock-Eval HI values of 238 mg HC/g rock on average indicate presence of Type II and III kerogen. The OM is immature as indicated by VR_r values between 0.3 and 0.5 %. Comparison with TOM concentrates, biomarker analysis, and microscopic observations indicate that kerogen quality determined by Rock-Eval® pyrolysis on whole rock powders might be severely underestimated for immature rock samples containing low-moderate TOC contents.

The restriction of potential source rock intervals to the eastern basins around the Troodos might be related to local and regional tectonic and paleo-geographic conditions, favoring enhanced bio-productivity in that area. Comparable situations might have also been present along the southeastern flank of the ESM. These young source rocks were definitely affected by strong biogenic gas generation during and after the Messinian. Such gas has high preservation potential due to its young state of generation and the presence of excellent cap rocks.

Acknowledgments

We thank the Ministry of Energy, Commerce, Industry and Tourism and the Geological Survey Department of Cyprus for the field work permission and their help in organization. Further, we gratefully acknowledge the support of Dr. Zomenia Zomeni and Dr. Efthymios Tsiolakis who assisted us during our field work and provided an excellent introduction into the regional geology of Cyprus. We thank the technical staff of IFPEN, Sorbonne Université and RWTH Aachen University, especially Dr. Alireza Baniasad, who provided helpful assistance with respect to analytical work. Finally, we want to thank Dr. Nikolaus Papadimitriou and Dr. Vasilis Symeou for fruitful discussions, which helped to better understand the geological history of Cyprus and two anonymous reviewers, who provided important and constructive comments on an earlier draft of this manuscript.

IFP Energies nouvelles provided financial support for the doctoral research of S. Grohmann.

References

Abed, A.M., Arouri, K.R., Boreham, C.J., 2005. Source rock potential of the phosphorite–bituminous chalk–marl sequence in Jordan. Marine and Petroleum Geology 22, 413-425.

Almogi-Labin, A., Bein, A., Sass, E., 1993. Late Cretaceous upwelling system along the southern Tethys margin (Israel): interrelationship between productivity, bottom water environments, and organic matter preservation. Paleoceanography 8, 671-690.

Barrier, E., Vrielynck, B., 2008. Atlas of Paleotectonic maps of the Middle East (MEBE Program). – CCGM – CGMW. - Atlas of 14 maps.

Behar, F., Beaumont, V., Penteado, H. D. B., 2001. Rock-Eval 6 technology: performances and developments. Oil & Gas Science and Technology 56, 111-134.

Berner, R. A., 1984. Sedimentary pyrite formation: an update. Geochimica et Cosmochimica Acta 48, 605-615.

Bertello F., Harby H., Brandolese S. (2016) Egypt: Zohr, an outstanding gas discovery in a new deep-water ydrocarbon play, In: 8th Mediterranean Offshore Conference and Exhibition, Alexandria, Egypt.

Bohacs, K.M., Carroll, A.R., Mankiewicz, P.J., Miskell-gerhardt, K.J., Schwalbach, J.O.N.R., Wegner, M.B., Simo, J.A.T., 2005. Production, destruction, and dilution-the many paths to source-rock development. in: Harris, N.B. (Ed.), The Deposition of Organic-carbon-rich Sediments: Models, Mechanisms and Consequences. Special Publications of SEPM, pp. 61-101.

Bou Daher, S., Ducros, M., Michel, P., Hawie, N., Nader, F. H., Littke, R., 2016. 3D thermal history and maturity modelling of the Levant Basin and its eastern margin, offshore–onshore Lebanon. Arabian Journal of Geosciences 9, 440.

Bou Daher, S., Nader, F. H., Müller, C., Littke, R., 2015. Geochemical and petrographic characterization of Campanian–Lower Maastrichtian calcareous petroleum source rocks of Hasbayya, South Lebanon. Marine and Petroleum Geology 64, 304-323.

Bou Daher, S., Nader, F. H., Strauss, H., Littke, R., 2014. Depositional environment and source-rock characterization of organic-matter rich Upper Santonian-Upper Campanian carbonates, northern Lebanon, Journal of Petroleum Geology 37, 5-24.

Bray, E. E., Evans, E. D., 1961. Distribution of n-paraffins as a clue to recognition of source beds. Geochimica et Cosmochimica Acta 22, 2-15.

Cyprus Geological Survey, 1995. Geological map of Cyprus, http://www.moa.gov.cy/moa/gsd/gsd.nsf/All/43CA34467BC412EAC2256FB30035287E/$file/

GeologicalMapOfCyprus_250k_en.jpg?OpenElement (accessed 13 September 2018 14:00), Cyprus Geological Survey, Nicosia, Cyprus.

Cyprus Mail, 2018. 'Zohr-like play' in Block 6, Turkish Navtex will not stop plans (Wrap-up), https://cyprus-mail.com/2018/02/08/zohr-like-play-block-6-turkish-navtex-will-not-stop-plans-wrap/ (accessed 13 September 2018 17:00), Cyprus Mail Company LTD., Nicosia, Cyprus.

Dean, W. E., Arthur, M. A., 1989. Iron-sulfur-carbon relationships in organic-carbon-rich sequences I: Cretaceous Western Interior Seaway. American Journal of Science 289, 708-743.

Dunham, R.J., 1962. Classification of Carbonate Rocks According to Depositional Texture. in: Ham, W.E. (Ed.), Classification of Carbonate Rocks, AAPG, Tulsa, pp. 108-121.

Durand, B. and Nicaise, G., 1980. Procedures for Kerogen Isolation. in: Durand, B. (Ed.), Kerogen Insoluble Organic Matter from Sedimentary Rocks, Editions Technip, Paris, pp. 35-53.

Eaton, S., Robertson, A., 1993. The Miocene Pakhna Formation, southern Cyprus and its relationship to the Neogene tectonic evolution of the Eastern Mediterranean. Sedimentary Geology 86, 273-296.

El Nady, M. M., 2007. Organic geochemistry of source rocks, condensates, and thermal geochemical modeling of Miocene sequence of some wells, onshore Nile Delta, Egypt. Petroleum science and technology 25, 791-818.

Esestime P., Hewitt A., Hodgson N. (2016) Zohr – a newborn carbonate play in the Levantine Basin, East-Mediterranean, First Break 34, 87–93.

Espitalié, J., Laporte, J. L., Madec, M., Marquis, F., Leplat, P., Paulet, J., Boutefeu, A., 1977. Méthode rapide de caractérisation des roches mètres, de leur potentiel pétrolier et de leur degré d'évolution. Revue de l'Institut français du Pétrole 32, 23-42.

Espitalié, J., Deroo, G., Marquis, F., 1986. La pyrolyse Rock-Eval et ses applications. Troisième partie. Revue de l'Institut français du Pétrole 41, 73-89.

Espitalié, J., Senga Makadi, K., Trichet, J., 1984. Role of the mineral matrix during kerogen pyrolysis. Organic Geochemistry 6, 365-382.

ExxonMobil, 2019. ExxonMobil makes natural gas discovery offshore Cyprus, https://corporate.exxonmobil.com/news/newsroom/news-releases/2019/0228_exxonmobil-makes-natural-gas-discovery-offshore-cyprus (accessed 3 April 2019 14:00), ExxonMobil Corporation, Texas, USA.

Feinstein, S., Aizenshtat, Z., Miloslavski, I., Gerling, P., Slager, J., McQuilken, J., 2002. Genetic characterization of gas shows in the east Mediterranean offshore of southwestern Israel. Organic Geochemistry 33, 1401-1413.

Galindo-Zaldivar, J., Nieto, L., Robertson, A., Woodside, J., 2001. Recent tectonics of Eratosthenes Seamount: an example of seamount deformation during incipient continental collision. Geo-Marine Letters 20, 233-242.

Gardosh, M. A., Druckman, Y., 2006. Seismic stratigraphy, structure and tectonic evolution of the Levantine Basin, offshore Israel. Geological Society, London, Special Publications 260, 201-227.

Gardosh, M., Druckman, Y., Buchbinder, B., Calvo, R., 2008. The Oligo-Miocene deepwater system of the Levant basin. Geological survey of Israel 33, 1-73.

Garfunkel, Z., 2004. Origin of the Eastern Mediterranean basin: a reevaluation. Tectonophysics 391, 11-34.

Ghalayini, R., Daniel, J. M., Homberg, C., Nader, F. H., Comstock, J. E., 2014. Impact of Cenozoic strike-slip tectonics on the evolution of the northern Levant Basin (offshore Lebanon). Tectonics 33, 2121-2142.

Ghalayini, R., Nader, F. H., Bou Daher, S., Hawie, N., Chbat, W. E., 2018. Petroleum systems of Lebanon: An update and review. Journal of Petroleum Geology 41, 189-214.

Granot, R., 2016. Palaeozoic oceanic crust preserved beneath the eastern Mediterranean. Nature Geoscience 9, 701.

Grohmann, S., Fietz, S. W., Littke, R., Daher, S. B., Romero-Sarmiento, M. F., Nader, F. H., Baudin, F., 2018. Source rock characterization of mesozoic to cenozoic organic matter rich marls and shales of the Eratosthenes Seamount, Eastern Mediterranean Sea. Oil & Gas Science and Technology–Revue d'IFP Energies nouvelles 73, 49.

Haq, B. U., Hardenbol, J., Vail, P. R., 1988. Mesozoic and Cenozoic chronostratigraphy and cycles of sea-level change. SEPM Special Publications 42.

Hawie, N., Deschamps, R., Nader, F. H., Gorini, C., Müller, C., Desmares, D., Hoteit, A., Granjeon, D., Montadert, L., Baudin, F., 2013a. Sedimentological and stratigraphic evolution of northern Lebanon since the Late Cretaceous: implications for the Levant margin and basin. Arabian Journal of Geosciences 7, 1323-1349.

Hawie, N., Gorini, C., Deschamps, R., Nader, F. H., Montadert, L., Granjeon, D., Baudin, F., 2013b. Tectono-stratigraphic evolution of the northern Levant Basin (offshore Lebanon). Marine and Petroleum Geology 48, 392-410.

Hawie, N., Deschamps, R., Granjeon, D., Nader, F. H., Gorini, C., Müller, C., Montadert, L., Baudin, F., 2017. Multi-scale constraints of sediment source to sink systems in frontier basins: a forward stratigraphic modelling case study of the Levant region. Basin Research 29, 418-445.

Henson, F. R. S., Browne, R. V., McGinty, J., 1949. A synopsis of the stratigraphy and geological history of Cyprus. Quarterly Journal of the Geological Society 105, 1-41.

Hsü, K. J., Montadert, L., Bernoulli, D., Cita, M. B., Erickson, A., Garrison, R. E., Kidd, R.B., Mélières, F., Müller, C., Wright, R., 1977. History of the Mediterranean salinity crisis. Nature, 267, 399-403.

Huang, W. Y., Meinschein, W. G., 1979. Sterols as ecological indicators. Geochimica et Cosmochimica Acta 43, 739-745.

Hunt, J. M., 1967. The origin of petroleum in carbonate rocks. in: Chilingar, G.V., Bissel, H.J., Fairbridge, R.W. (Eds.) Developments in Sedimentology 9B. Carbonate Rocks: Elsevier, New York, pp. 225-251.

Inati, L., Zeyen, H., Nader, F. H., Adelinet, M., Sursock, A., Rahhal, M. E., Roure, F., 2016. Lithospheric architecture of the Levant Basin (Eastern Mediterranean region): A 2D modeling approach. Tectonophysics 693, 143-156.

Inati, L., Lecomte, J. C., Zeyen, H., Nader, F. H., Adelinet, M., Rahhal, M. E., Sursock, A., 2018. Crustal configuration in the northern Levant basin based on seismic interpretation and numerical modeling. Marine and Petroleum Geology 93, 182-204.

Katz, B. J., 1983. Limitations of 'Rock-Eval'pyrolysis for typing organic matter. Organic Geochemistry 4, 195-199.

Katz, B. J., 2012. Petroleum source rocks. Springer Science & Business Media, Berlin.

Kähler, G., 1994. Stratigraphy and sedimentology of the Lefkara formation, Cyprus (Palaeogene to Early Neogene). PhD thesis, Department of Geology, University of Southampton.

Kähler, G., Stow, D. A., 1998. Turbidites and contourites of the Palaeogene Lefkara Formation, southern Cyprus. Sedimentary Geology 115, 215-231.

Kinnaird, T. C., Robertson, A. H., Morris, A., 2011. Timing of uplift of the Troodos Massif (Cyprus) constrained by sedimentary and magnetic polarity evidence. Journal of the Geological Society 168, 457-470.

Kouwenhoven, T. J., Van der Zwaan, G. J., 2006. A reconstruction of late Miocene Mediterranean circulation patterns using benthic foraminifera. Palaeogeography, Palaeoclimatology, Palaeoecology 238, 373-385.

Krijgsman, W., Blanc-Valleron, M. M., Flecker, R., Hilgen, F. J., Kouwenhoven, T. J., Merle, D., Orszag-Sperber, F., Rouchy, J. M., 2002. The onset of the Messinian salinity crisis in the Eastern Mediterranean (Pissouri Basin, Cyprus). Earth and Planetary Science Letters 194, 299-310.

Lapierre, H., 1975. Les formations sédimentaires et éruptives des nappes de Mamonia et leurs relations avec le Massif du Troodos (Chypre occidentale). Mémoires de la Société géologique de France no. 123, pp. 131. ISBN-10: 2704000549.

Lapierre, H., Bosch, D., Narros, A., Mascle, G. H., Tardy, M., Demant, A., 2007. The Mamonia Complex (SW Cyprus) revisited: remnant of Late Triassic intra-oceanic volcanism along the Tethyan southwestern passive margin. Geological Magazine 144, 1-19.

Lewan, M. D., 1984. Factors controlling the proportionality of vanadium to nickel in crude oils. Geochimica et Cosmochimica Acta, 48, 2231-2238.

Littke R., 1993. Deposition, diagenesis and weathering of organic matter-rich sediments. in: Fairchild, I. (Ed.) Lecture Notes in Earth Sciences, Springer, Berlin, pp. 22-27, pp. 169-182. ISBN: 3540573860.

Littke, R., Sachsenhofer, R. F., 1994. Organic petrology of deep sea sediments: a compilation of results from the Ocean Drilling Program and the Deep Sea Drilling Project. Energy & fuels 8, 1498-1512.

Lord, A. R., Panayides, I., Urquhart, E., Xenophontos, C., Malpas, J., 2000. A biochronostratigraphical framework for the Late Cretaceous–Recent circum-Troodos sedimentary sequence, Cyprus, in: Proceedings of the Third International Conference on the Geology of the Eastern Mediterranean. Geological Survey Department, Nicosia, Vol. 289, pp. 297, ISBN: 9963175066.

Makris, J., Stobbe, C., 1984. Physical properties and state of the crust and upper mantle of the Eastern Mediterranean Sea deduced from geophysical data. Marine Geology 55, 347-363.

Meilijson, A., Steinberg, J., Hilgen, F., Bialik, O. M., Waldmann, N. D., Makovsky, Y., 2018. Deep-basin evidence resolves a 50-year-old debate and demonstrates synchronous onset of Messinian evaporite deposition in a non-desiccated Mediterranean. Geology 46, 243-246.

Montadert L., Nicolaides S., Semb P.H., Lie Ø., 2014. Petroleum Systems Offshore Cyprus, in: Marlow L., Kendall C., Yose L. (Eds.), AAPG Special Volumes Memoir 160: Petroleum systems of the Tethyan region, AAPG, Tulsa, OK, pp. 301-334.

Nader, F.H., 2014. Insights into the petroleum prospectivity of Lebanon, in: L. Marlow, C. Kendall and L. Yose (Eds.), Petroleum systems of the Tethyan region: AAPG Memoir 106, pp. 241–278.

National Oceanic and Atmospheric Administration, 2018. Bathymetric Data Viewer, https://maps.ngdc.noaa.gov/viewers/bathymetry/ (accessed 28 November 2018 11:00), National Centers for Environmental Information, U.S. Department of Commerce, Washington, D.C., USA.

Nixon, S. W., Oviatt, C. A., Frithsen, J., & Sullivan, B., 1986. Nutrients and the productivity of estuarine and coastal marine ecosystems. Journal of the Limnological Society of Southern Africa 12, 43-71.

Papadimitriou, N., Gorini, C., Nader, F. H., Deschamps, R., Symeou, V., Lecomte, J. C., 2018. Tectono-stratigraphic evolution of the western margin of the Levant Basin (offshore Cyprus). Marine and Petroleum Geology 91, 683-705.

Peters, K. E., 1986. Guidelines for evaluating petroleum source rock using programmed pyrolysis. AAPG bulletin 70, 318-329.

Peters, K. E., Walters, C. C., Moldowan, J. M., 2005. The biomarker guide: Volume 1, Biomarkers and isotopes in the environment and human history. Cambridge University Press, New York, ISBN: 0521781582.

Peters, K. E., Walters, C. C., Moldowan, J. M., 2007. The biomarker guide: Volume 2, Biomarkers and isotopes in petroleum systems and earth history. Cambridge University Press, NewYork, ISBN:9780521039987.

Racka, M., Marynowski, L., Filipiak, P., Sobstel, M., Pisarzowska, A., Bond, D. P., 2010. Anoxic Annulata events in the Late Famennian of the Holy Cross Mountains (Southern Poland): geochemical and palaeontological record. *Palaeogeography, Palaeoclimatology, Palaeoecology* 297, 549-575.

Ratner M., 2016. Natural Gas Discoveries in the Eastern Mediterranean, Congressional Research Service, Washington, D.C., pp. 1-15.

Regelous, M., Haase, K. M., Freund, S., Keith, M., Weinzierl, C. G., Beier, C., Brandl, P.A., Endres, T., Schmidt, H., 2014. Formation of the Troodos Ophiolite at a triple junction: Evidence from trace elements in volcanic glass. Chemical Geology 386, 66-79.

Reiche, S., Hübscher, C., Ehrhardt, A., 2016. The impact of salt on the late Messinian to recent tectonostratigraphic evolution of the Cyprus subduction zone. Basin Research 28, 569-597.

Ricken, W.,1993. Sedimentation as a three-component system. Organic carbon, carbonate, noncarbonated. in: Fairchild, I. (Ed.) *Lecture Notes in Earth Sciences, Volume 51,Springer*, Berlin, pp. 358, ISBN: 3540573860.

Robertson, A. H. F., Woodcock, N. H., 1979. Mamonia Complex, southwest Cyprus: Evolution and emplacement of a Mesozoic continental margin. Geological Society of America Bulletin 90, 651-665.

Robertson, A. H., Parlak, O., Ustaömer, T., 2012. Overview of the Palaeozoic–Neogene evolution of neotethys in the Eastern Mediterranean region (Southern Turkey, Cyprus, Syria). Petroleum Geoscience 18, 381-404.

Robertson, A. H., 1998. Mesozoic-Tertiary tectonic evolution of the easternmost Mediterranean area: integration of marine and land evidence. Proceedings of the Ocean Drilling Program, Scientific Results, Vol. 160; Chapter 54, 723-782.

Rohling, E. J., Marino, G., Grant, K. M., 2015. Mediterranean climate and oceanography, and the periodic development of anoxic events (sapropels). Earth-Science Reviews 143, 62-97.

Sachse, V. F., Littke, R., Heim, S., Kluth, O., Schober, J., Boutib, L., Jabour, H., Perssen, F., Sindern, S., 2011. Petroleum source rocks of the Tarfaya Basin and adjacent areas, Morocco. Organic Geochemistry 42, 209-227.

Schneider, F., Dubille, M., Montadert, L., 2016. Modeling of microbial gas generation: application to the eastern Mediterranean “Biogenic Play”. Geologica Acta 14, 403-417.

Segev, A., Rybakov, M., 2010. Effects of Cretaceous plume and convergence, and Early Tertiary tectonomagmatic quiescence on the central and southern Levant continental margin. Journal of the Geological Society 167, 731-749.

Senftle, J. T., Brown, J. H., Larter, S. R., 1987. Refinement of organic petrographic methods for kerogen characterization. International Journal of Coal Geology 7, 105-117.

Shaaban, F., Lutz, R., Littke, R., Bueker, C., Odisho, K., 2006. Source-rock evaluation and basin modelling in NE Egypt (NE Nile delta and Northern Sinai). Journal of Petroleum Geology 29, 103-124.

Stock, A.T., Littke, R., Schwarzbauer, J., Horsfield, B., Hartkopf-Fröder, C., 2017. Organic geochemistry and petrology of Posidonia Shale (Lower Toarcian, Western Europe) - The evolution from immature oil-prone to overmature dry gas-producing kerogen. International Journal of Coal Geology, 176-177, 36-48.

Swarbrick, R. E., Robertson, A. H. F., 1980. Revised stratigraphy of the Mesozoic rocks of southern Cyprus. Geological Magazine 117, 547-563.

Symeou V., Homberg C., Nader F. H., Darnault R., Lecomte J. C., Papadimitriou N., 2018. Longitudinal and Temporal Evolution of the Tectonic Style Along the Cyprus Arc System, Assessed Through 2-D Reflection Seismic Interpretation, Tectonics 37, 30-47.

Szczepanik, P., Witkowska, M., Sawłowicz, Z., 2010. Geochemistry of Middle Jurassic mudstones (Kraków-Częstochowa area, southern Poland): interpretation of the depositional redox conditions. Geological Quarterly 51, 57-66.

Taylor, G.H., Teichmüller, M., Davis, A., Diessel, C.F.K., Littke, R., Robert, P., 1998. Organic Petrology. Gebrüder Bornträger, Berlin, Stuttgart, pp. 704, ISBN: 3443010369.

Tyson, R. V., 1995. Palynological kerogen classification, in: Sedimentary Organic Matter, Springer, Dordrecht, pp. 341-365.

Wigger, S., Bailey, J., Larsen, M., Wallace, M., 1997. Ha'py field: a Pliocene bright spot example from the Nile delta, Egypt. The Leading Edge 16, 1827–1829.

Wignall, P. B., Newton, R., 1998. Pyrite framboid diameter as a measure of oxygen deficiency in ancient mudrocks. American Journal of Science 298, 537-552.

Wilkin, R. T., Arthur, M. A., Dean, W. E. 1997. History of water-column anoxia in the Black Sea indicated by pyrite framboid size distributions. *Earth and Planetary Science Letters 148*, 517-525.

Wilkin, R. T., Barnes, H. L. 1996. Pyrite formation by reactions of iron monosulfides with dissolved inorganic and organic sulfur species. *Geochimica et Cosmochimica Acta 60*, 4167-4179.

Van der Zwaan, G. J., Jorissen, F. J., 1991. Biofacial patterns in river-induced shelf anoxia. Geological Society, London, Special Publications 58, 65-82.

Zieger, L., Littke, R., Schwarzbauer, J., 2018. Chemical and structural changes in vitrinites and megaspores from Carboniferous coals during maturation. International Journal of Coal Geology 185, 91-102.

Figure captions

Figure 1

A) Overview of the Eastern Mediterranean Sea showing the recent tectonic setting. The study area is located at the triple-junction point between the African, the Arabian and the Eurasian plates. White arrows indicate movement orientation of the African and Arabian plates relative to Eurasia (fault location according to Symeou et al., 2018), ESM = Eratosthenes Seamount, B) Overview of the study area showing a simplified geological map of Cyprus (modified after the official geological map, Cyprus Geological Survey, 1995) and the surrounding basins and the ESM. Yellow dots show the Ocean Drilling Program (ODP) Leg 160 wells (see Grohmann et al. (2018) for respective offshore samples). White (TOC < 0.3 wt.%) and black dots (TOC > 0.3 wt.%) show onshore sample locations. (for all locations and GPS coordinates, see Table 1). Bathymetric and topographic maps taken from the National Oceanic and Atmospheric Administration (2018) Bathymetric Data Viewer. Fm. = Formation.

Figure 2

Simplified lithostratigraphy of southern Cyprus as it can be observed within the different sub-basins (modified after Kinnaird et al., 2011) and the main tectonic events. Proposed estimated thicknesses are speculative and must be treated with caution as they can vary throughout each basin. Note that the Mamonia Complex (C.) does not apply to the time scale, as it represents an allochthonous mélange that was overthrusted onto the Troodos Ophiolite (its rocks span ages from Triassic to Late Cretaceous). Green stars mark sampled intervals.

Figure 3

Sedimentological and geochemical logs of the Mid Triassic Vlambouros Formation (Fm). at location 31 and 32 (For locations see Figure 1 and Table 1). Coloring of the lithological column indicates observed rock color. Horizontal lines indicate recognizable normal

lamination, while inclined lines indicate cross bedding. Although the clay-rich sections partly show elevated total organic carbon (TOC) contents, the source rock quality is poor due to low hydrogen index (HI) values < 50 mg HC/g TOC on average. Total sulfur (TS)/TOC ratios indicate oxic conditions during deposition (Berner, 1984). TS/Fe ratios indicate that most sulfur is bound to pyrite. White line and arrow indicates small normal fault observed in the outcrop.

Figure 4

Sedimentological and geochemical logs of the Late Miocene Upper Pakhna Formation at location 1 and 10 (for locations see Figure 1 and Table 1). Coloring of the lithological column indicates observed rock color. Total organic (TOC) and inorganic carbon (TIC) contents and hydrogen index (HI) values indicate good source rock quality. Total sulfur (TS)/Fe ratios show that all sulfur is bound to pyrite. TS/TOC ratios are mainly lower than those observed under normal marine conditions, suggesting a deposition under anoxic conditions (Berner, 1984).

Figure 5

Rock-Eval® results for all > 0.3 wt.% total organic carbon (TOC) samples. A) Pseudo-van Krevelen diagram (Hydrogen Index (HI) vs. Oxygen Index (OI)) after Espitallié et al. (1986). B) Rock-Eval® T_{max} vs. HI plot to avoid misinterpretation related to probably inaccurate OI values. In both plots, the majority of the Pakhna samples is interpreted as Type II kerogen while the Vlambouros samples are Type III. However, some Pakhna samples (mainly from Location (Loc.) 2, 11, 20, and 21) also plot as Type III kerogen, although their depositional setting is supposed to be marine.

Figure 6

Reflected light (A, C, E, G, H, I, J) and fluorescence (B, D, F) microphotographs. A and B) Representative sample for the organic-rich sections of the Pakhna Formation (Fm.) from location (Loc.) 10. The sample is composed of a fine-grained siliciclastic matrix with patchy carbonate (carb). Pyrite (py) is mainly present as framboids. Organic matter (OM) is mainly present as fine, disseminated liptinites (Lipt) as indicated by the yellowish background fluorescence (B). Only small amounts of terrestrial particles such as vitrinites (Vit) can be observed. The OM as well as the pyrite framboids seem to be more abundant in the more siliciclastic parts, while foraminifera (foram) can rather be observed in the more calcareous parts. C and D) Representative sample for the organic-rich sections of the Pakhna Fm. from Loc. 1. Additionally to liptodetrinite, alginites can be observed parallel to the bedding planes. Many pyrite framboids show diameters > 5µm. OM seems to be related to the more clastic parts. E and F) Representative sample of the less organic-rich samples of the Pakhna Fm. from the southwestern outcrops (Loc. 11, 12, 20, 21). The samples are characterized by more calcareous deposits and a reduced abundance of amorphous liptinites. Alginites can still be observed but are here also present in the calcareous parts (F). G and H) Sample 228 is the only sample from the Pakhna Fm. where intense pyrite weathering could be observed. The pyrite is partly present as pore filling within foraminifera. I & J) Large vitrinite (Vit) and intertinites (Inert) particles with recognizable cell structures in the Vlambouros Fm. at Loc. 32 and 24, respectively.

Figure 7

A and B) Comparison of Rock-Eval® pyrograms for the bulk rock (BR) and the respective total organic matter (TOM) concentrates of two Pakhna samples. For comparison, the curves are normalized to the sample weight and the respective total organic carbon (TOC) content. A) It can be seen that a large proportion of the thermovaporized and pyrolyzable hydrocarbon (HC) is retained by the mineral matrix. B) The effect is even more prominent if the bulk TOC is lower. C) The absolute difference between bulk and TOM HI and OI in the Pakhna samples seems to decrease with increasing bulk TOC content. D) The Pakhna TOM

concentrates plot closer to the kerogen Type II pathway than the respective bulk rock samples in the pseudo van Krevelen diagram and correlate better with the elemental results (E). Loc. = Location.

Figure 8

Several thermal maturity parameters. A) Random vitrinite reflectance (VR_r) and Rock-Eval® T_{max} values indicate an immature state of organic matter with only the Vlambouros samples reaching up to early maturity. B) The configuration of 20S/(20S+20R) and αββ/(ααα+αββ) regular steranes indicates an immature to early mature state for all samples.

Figure 9

Distribution of organic molecular compounds in the aliphatic fraction of representative samples of the Pakhna Formation (Fm.) from location (Loc.) 1 and 10 in the northeast (sample 20), and from the southwest (sample 233), and of the Vlambouros Fm. (sample 250). A) Representative full chromatograms (GC-FID) showing distribution of *n*-alkanes and pristane (Pr) and phytane (Ph). B) Mass chromatograms m/z 191 of the aliphatic fraction showing distribution of hopanes. C) Mass chromatograms m/z 217 showing distribution of steranes.

Figure 10

Transmitted light microphotographs of palynological components. The general palynofacies of the Pakhna samples is represented by A and B: The largest percentage (up to >90 %) is made up by amorphous organic matter (AOM) of dark brownish color which forms large, clumpy aggregates. Minor components include different types of pollen (A and C), highly oxidized palynomacerals (PM4) and algae. The Vlambouros samples are almost exclusively characterized by oxidized PM (D). For the statistical overview of the different compounds see Figure 11.

Figure 11

Results of the palynological observations. Values expressed in wt.% indicates the total organic carbon (TOC) content of the respective sample. The Pakhna samples are mainly (up to > 90 %) composed of amorphous organic matter (AOM). Terrestrial particles like palynomacerals (PM) are highly oxidized (mainly PM4 and PM1). Other terrestrial and marine constituents like spores, pollen, algae, and foraminifera are relatively constant to each other. Samples containing low TOC show also a decrease in the percentage of AOM. In the Vlambouros samples the OM is almost exclusively (>90 %) composed of highly oxidized PM.

Figure 12

Results of the pyrite framboid size distribution in Pakhna samples originating from location 10. A) Histograms showing the distribution of pyrite framboid diameters (bin size = 1 µm). n = number of measured framboids, mean = mean framboid diameter, std = standard deviation to mean value, skew = skewness of distribution. B) and C) plot of the mean framboid diameters vs. the standard deviation and skewness of the distribution, respectively, pointing towards euxinic/anoxic conditions (plots after Wilkins et al., 1996).

Figure 13

Ternary diagram showing the original sediment composition calculated according to Littke (1993) under the assumption that all sulfur now present as pyrite/marcasite is derived from early diagenetic sulfate reduction and organic carbon oxidation. 2 moles carbon are lost in order to create one mole of (reduced) sulfur: TOC* = TOC x 2S x (M_C/M_S) with TOC*: TOC (total organic carbon) before bacterial sulfate reduction, S: sulfur content, M_C and M_S: molar mass of carbon and sulfur, respectively. OM* = TOC* x (C_{OM}) with OM* = original organic matter, C_{OM}: carbon percentage in the OM (here an average of 70% is assumed for marine

organic matter; see Stock et al., 2017). In the Littke plot, the carbon (Carb) content is determined based on the elemental carbon analysis and the silicate (Sil) content is calculated as Sil = 100 - %OM* - %Carb. The Pakhna samples (especially samples from the northeastern locations (Loc.) 1 and 10) show a tendency to increasing OM with increasing silicate and decreasing carbonate content, respectively, while the OM in the Vlambouros samples shows no correlation.

Figure 14

Various elemental ratios to interpret paleo-redox conditions. A) D) Total sulfur (TS) vs. total organic carbon (TOC) contents (Berner, 1984). B) TS vs. vanadium-nickel fraction (V/(Ni+V)). The three fields with the roman numbers correspond to the stability regimes of different species as proposed by Lewan (1984). C) Ternary diagram showing the relative concentration of total organic carbon (TOC), total sulfur (TS) and iron (Fe). Diagram after Dean and Arthur (1989) and Racka et al. (2010). For samples which have excess iron, it can be assumed that most sulfur is incorporated in pyrite. In total, the Pakhna samples are interpreted as dys- to anoxic conditions, while the samples of the Vlambouros Fm. are related to oxic, sulfate-depleted conditions.

Figure 15

Various biomarker ratios to determine source of organic matter (OM) and paleo redox-conditions. A) Pristane (Pr) over *n*-C_{17} vs. Phytane (Ph) over *n*-C_{18} indicating oxygen depleted conditions for the Pakhna samples. Samples from Location (Loc.) 1 and 10 seem to be slightly more oxygen depleted then samples from the other outcrops. The samples of the Vlambouros Formation (Fm.) indicate more oxic conditions. B) Pr/n-C_{17} vs. Pr/Ph indicating a mainly marine/aquatic source of OM for Pakhna samples from Loc. 1 and 10, while the other Pakhna samples as well as the Vlambouros samples indicate also a contribution of terrestrial

OM. C) The ratio of C_{29} to C_{27} regular steranes, however, indicates for all samples a mainly marine algal source. D) According to the ratio of tricyclic hopanes C_{24}/C_{23} vs. C_{22}/C_{21} the depositional setting is to interpret as somewhat between a marly-carbonaceous source and a more marine or freshwater dominated environment. Loc. = Location.

Figure 16

Relative distribution of C_{27} to C_{29} regular steranes showing a mainly marine source of organic matter (OM) for the Pakhna samples and partly increased terrestrial influence in the Vlambouros samples. Paleoenvironmental and source interpretation after Huang and Meinschein, 1979). Loc. = Location.

Table captions

Table 1

List of investigated locations and the respective formation, taken samples and GPS coordinates. Locations where organic matter could be proven are marked by *. Locations are shown on the geological map (Fig. 1) and in the lithostratigraphic column (Fig. 2).

Table 2

Total organic (TOC) and inorganic carbon (TIC) and Rock-Eval® results for bulk rock samples > 0.3 wt.% TOC. For locations (Loc.) see Fig. 1 and 2. Fm. = Formation, P = Pakhna; V = Vlambouros, [---] = T_{max} was not determined due to bad resolution of the S2 peak. HI = hydrogen index, OI = oxygen index, T_{max} = temperature at S2 peak.

Table 3

Comparison of Rock-Eval® results obtained from bulk rock samples and the respective total organic matter concentrates. TOC = total organic carbon, HI = hydrogen index, OI = oxygen index, T_{max} = temperature at S2 peak.

Table 4

Average random vitrinite reflectance (VR_r) for each outcrop based on one or several samples ($n_{samples}$). Fm. = Formation (P = Pakhna, V = Vlambouros); Loc. = Location; n_{total} = total amount of measured vitrinite particles per outcrop; Std dev = standard deviation.

Table 5

Various molecular ratios calculated from the saturated hydrocarbon fraction. Loc. = Location, Fm. = Formation (P = Pakhna, V = Vlambouros).

Table 6

Hopane and sterane ratios obtained from the saturated fraction. [---] = no results obtained. Loc. = Location, Fm. = Formation (P = Pakhna, V = Vlambouros).

Table 7

Elemental concentrations in the bulk rock samples. [---] = not measured. Loc. = Location, Fm. = Formation (P = Pakhna, V = Vlambouros), TS = total sulfur, Fe = iron, Ni = nickel, V = vanadium.

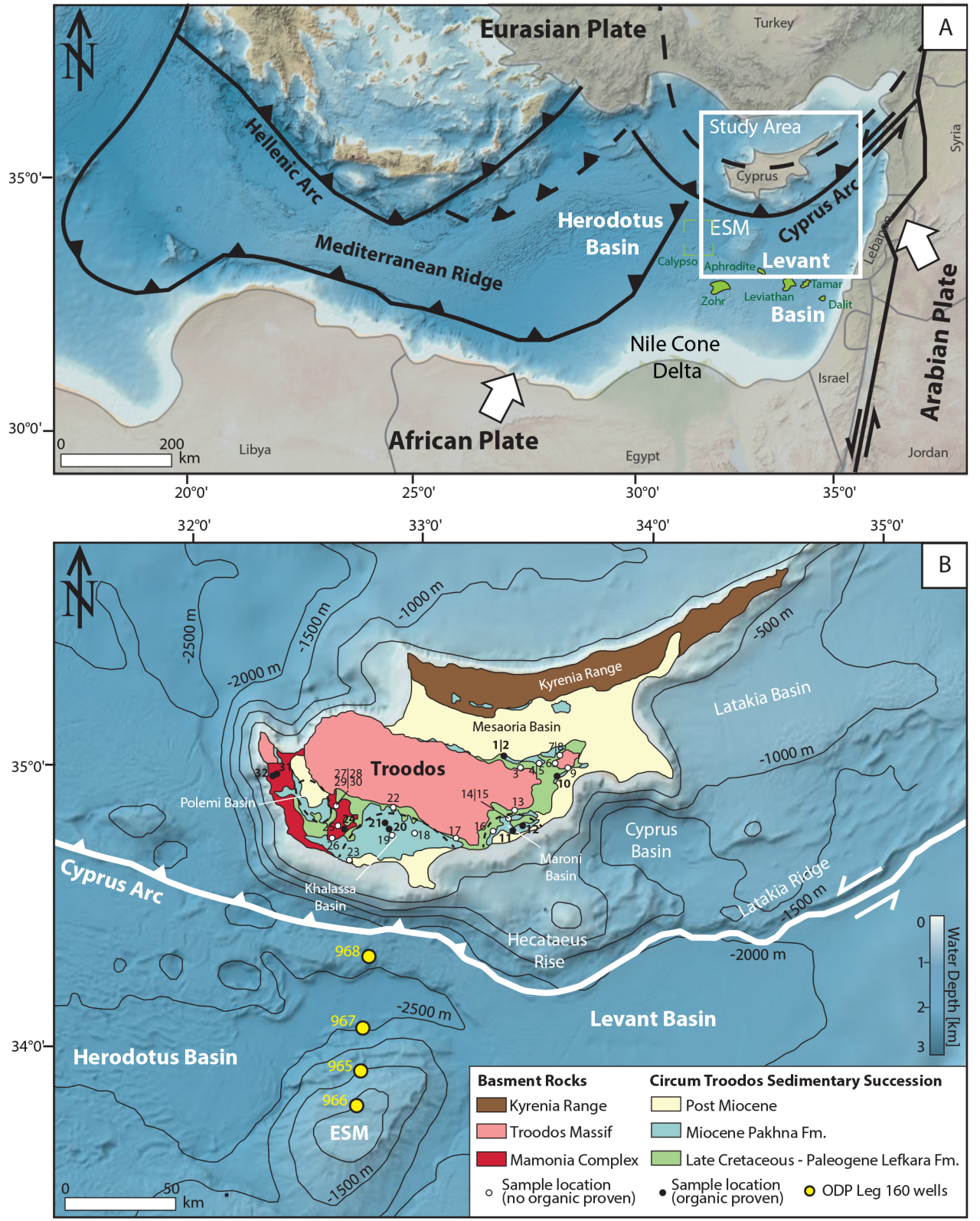
A
Eurasian Plate
Turkey
Hellenic Arc
Mediterranean Ridge
Herodotus Basin
Study Area
Cyprus
Cyprus Arc
Syria
ESM
Calypso
Aphrodite
Levant
Basin
Tamar
Leviathan
Zohr
Dalit
Lebanon
Arabian Plate
Nile Cone
Delta
Israel
African Plate
Libya
Egypt
Jordan
0
200
km
35°0'
30°0'
20°0'
25°0'
30°0'
35°0'
32°0'
33°0'
34°0'
35°0'
B
-2500 m
-2000 m
-1500 m
-1000 m
-500 m
Kyrenia Range
Mesaoria Basin
Troodos
Latakia Basin
Polemi Basin
Cyprus Arc
Khalassa
Basin
Maroni
Basin
Cyprus
Basin
Latakia Ridge
Hecataeus
Rise
Levant Basin
Herodotus Basin
ESM
968
967
965
966
0
50
km
Water Depth [km]
Basment Rocks
Kyrenia Range
Troodos Massif
Mamonia Complex
Circum Troodos Sedimentary Succession
Post Miocene
Miocene Pakhna Fm.
Late Cretaceous - Paleogene Lefkara Fm.
Sample location (no organic proven)
Sample location (organic proven)
ODP Leg 160 wells

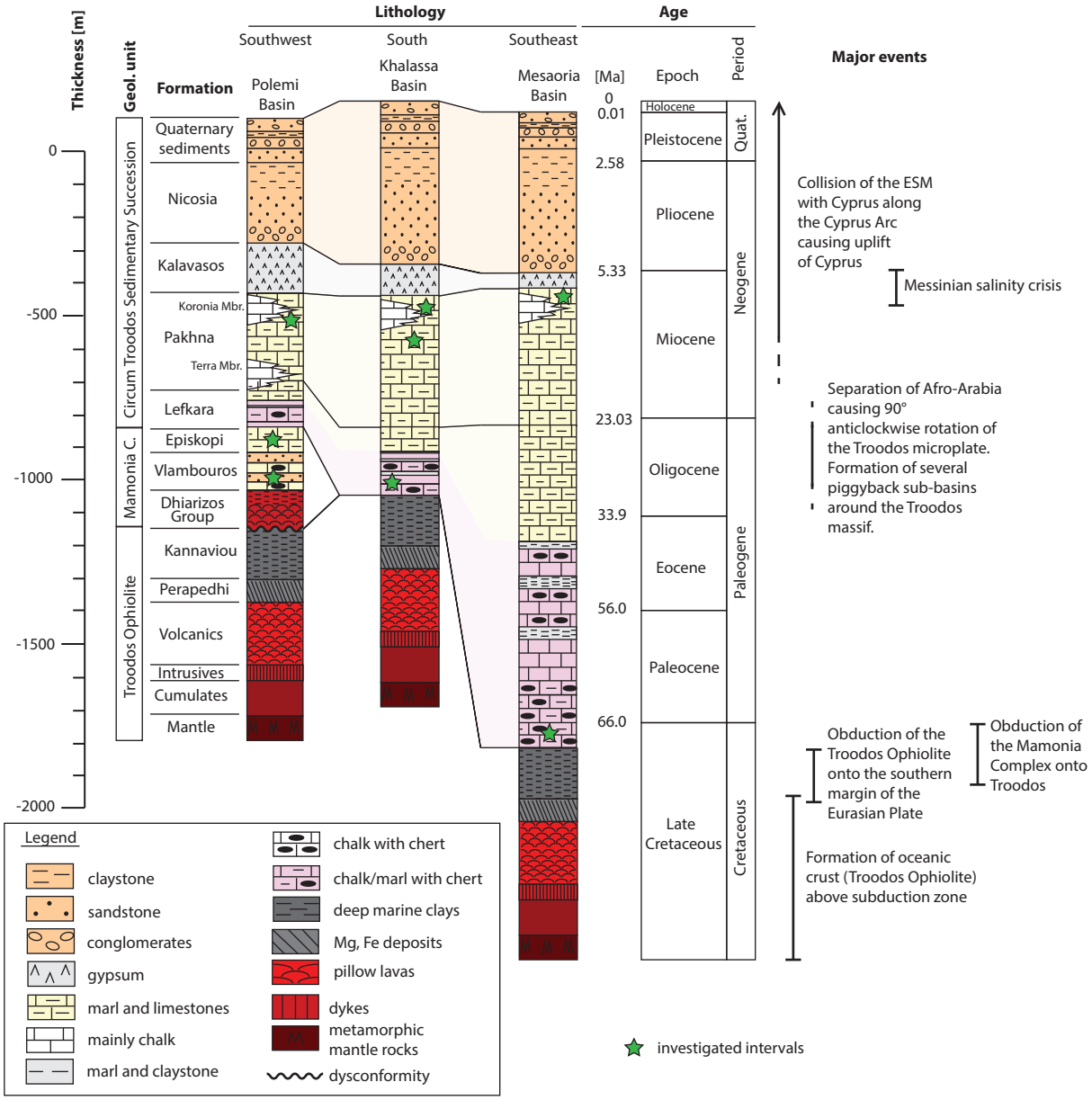
Lithology
Age
Southwest
South
Southeast
Thickness [m]
Geol. unit
Formation
Polemi Basin
Khalassa Basin
Mesaoria Basin
[Ma]
Epoch
Period
Major events
0
-500
-1000
-1500
-2000
Circum Troodos Sedimentary Succession
Mamonia C.
Troodos Ophiolite
Quaternary sediments
Nicosia
Kalavasos
Koronia Mbr.
Pakhna
Terra Mbr.
Lefkara
Episkopi
Vlambouros
Dhiarizos Group
Kannaviou
Perapedhi
Volcanics
Intrusives
Cumulates
Mantle
0
0.01
2.58
5.33
23.03
33.9
56.0
66.0
Holocene
Pleistocene
Pliocene
Miocene
Oligocene
Eocene
Paleocene
Late Cretaceous
Quat.
Neogene
Paleogene
Cretaceous
Collision of the ESM with Cyprus along the Cyprus Arc causing uplift of Cyprus
Messinian salinity crisis
Separation of Afro-Arabia causing 90° anticlockwise rotation of the Troodos microplate. Formation of several piggyback sub-basins around the Troodos massif.
Obduction of the Troodos Ophiolite onto the southern margin of the Eurasian Plate
Obduction of the Mamonia Complex onto Troodos
Formation of oceanic crust (Troodos Ophiolite) above subduction zone
Legend
claystone
sandstone
conglomerates
gypsum
marl and limestones
mainly chalk
marl and claystone
chalk with chert
chalk/marl with chert
deep marine clays
Mg, Fe deposits
pillow lavas
dykes
metamorphic mantle rocks
dysconformity
investigated intervals

Location 31: Vlambouros Fm.

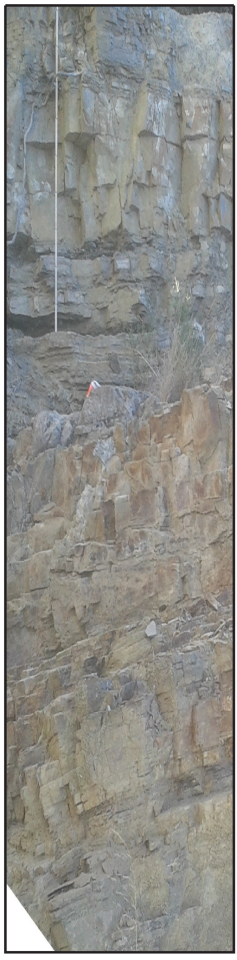

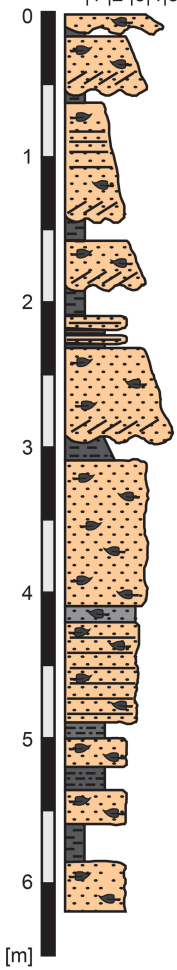

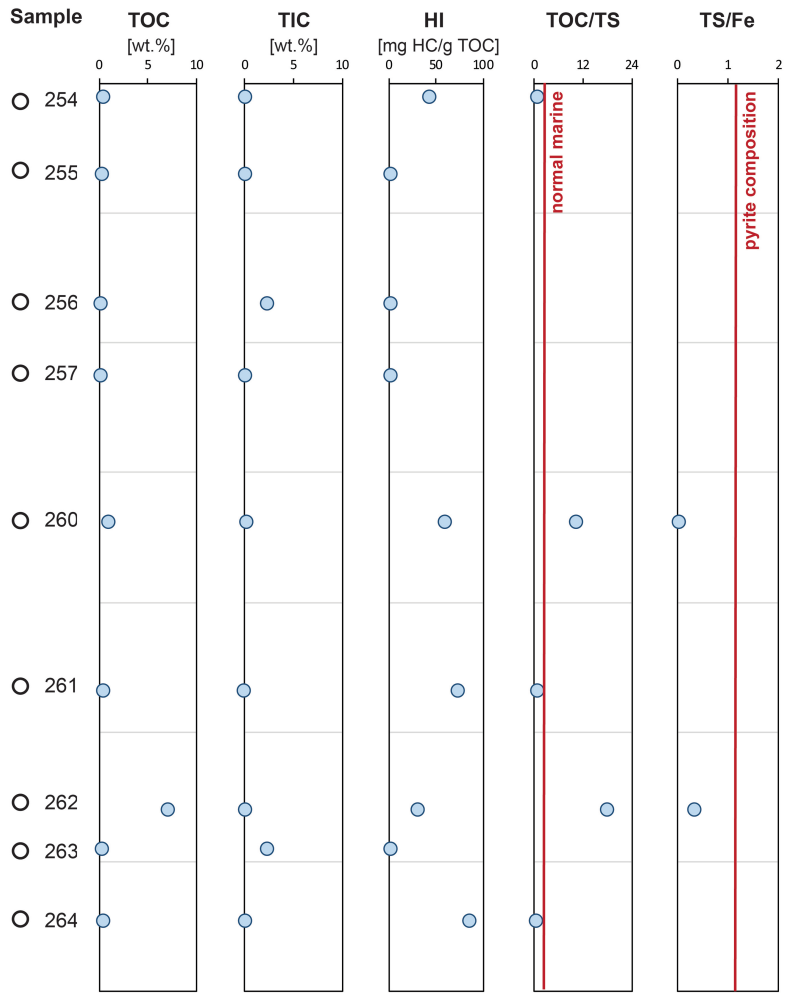

1: Clay, 2: Silt, 3: Fine- , 4:Medium-, 5:Coarse-sand — Plant debris

Location 32: Vlambouros Fm.

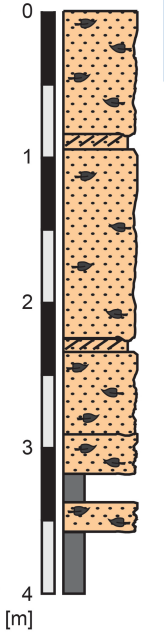

1: Clay, 2: Silt, 3: Fine-sand — Plant debris

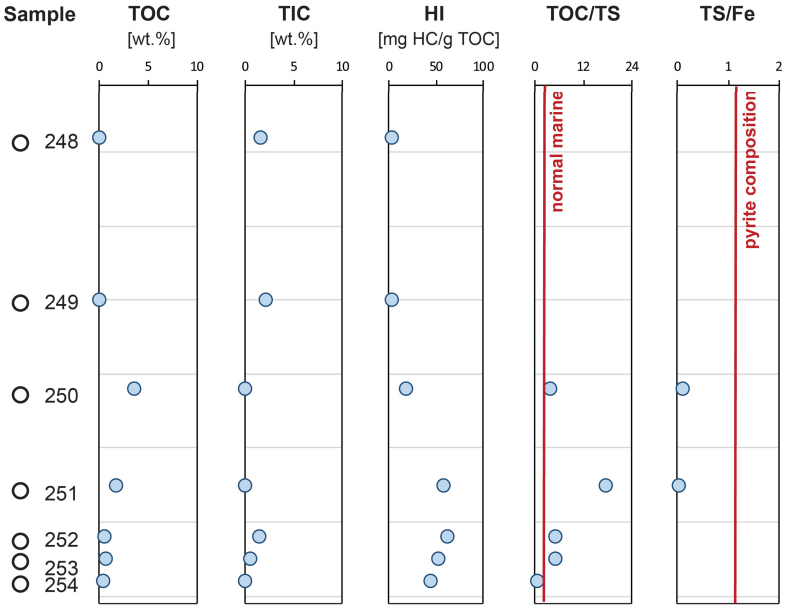

Location 1: Pakhna Fm.

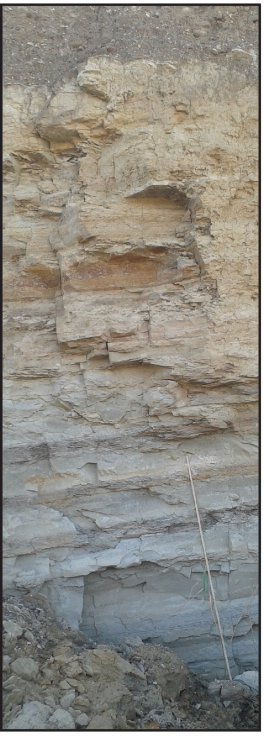

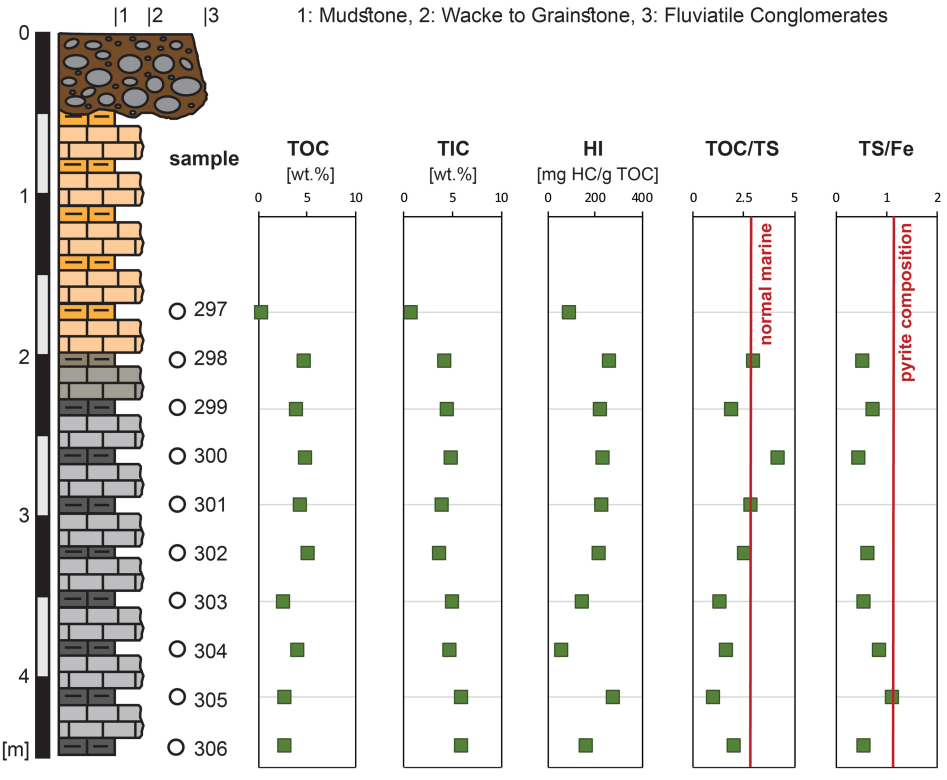

Location 10: Pakhna Fm.

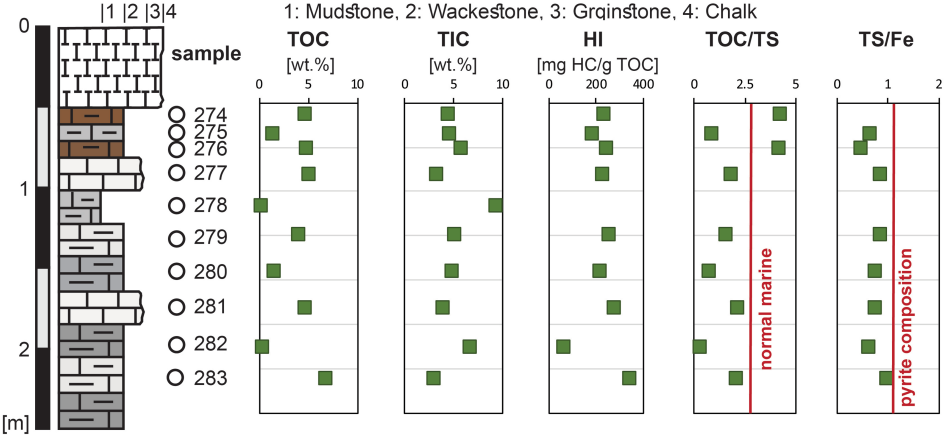

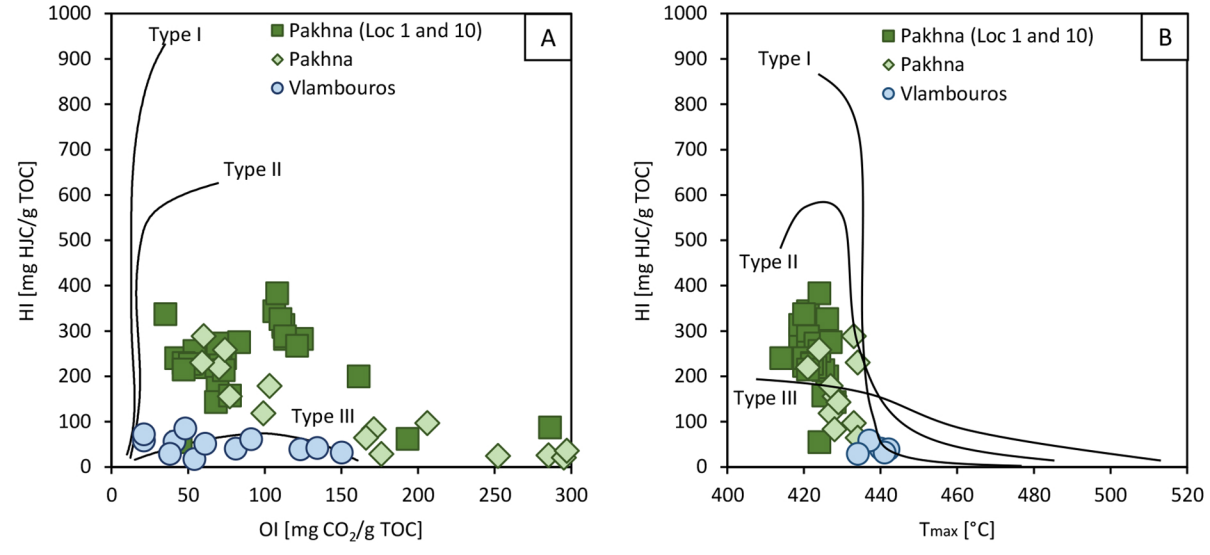
A
Type I
Type II
Type III
Pakhna (Loc 1 and 10)
Pakhna
Vlambouros
HI [mg HJC/g TOC]
OI [mg CO2/g TOC]
0
100
200
300
400
500
600
700
800
900
1000
0
50
100
150
200
250
300
B
Type I
Type II
Type III
Pakhna (Loc 1 and 10)
Pakhna
Vlambouros
HI [mg HJC/g TOC]
Tmax [°C]
400
420
440
460
480
500
520

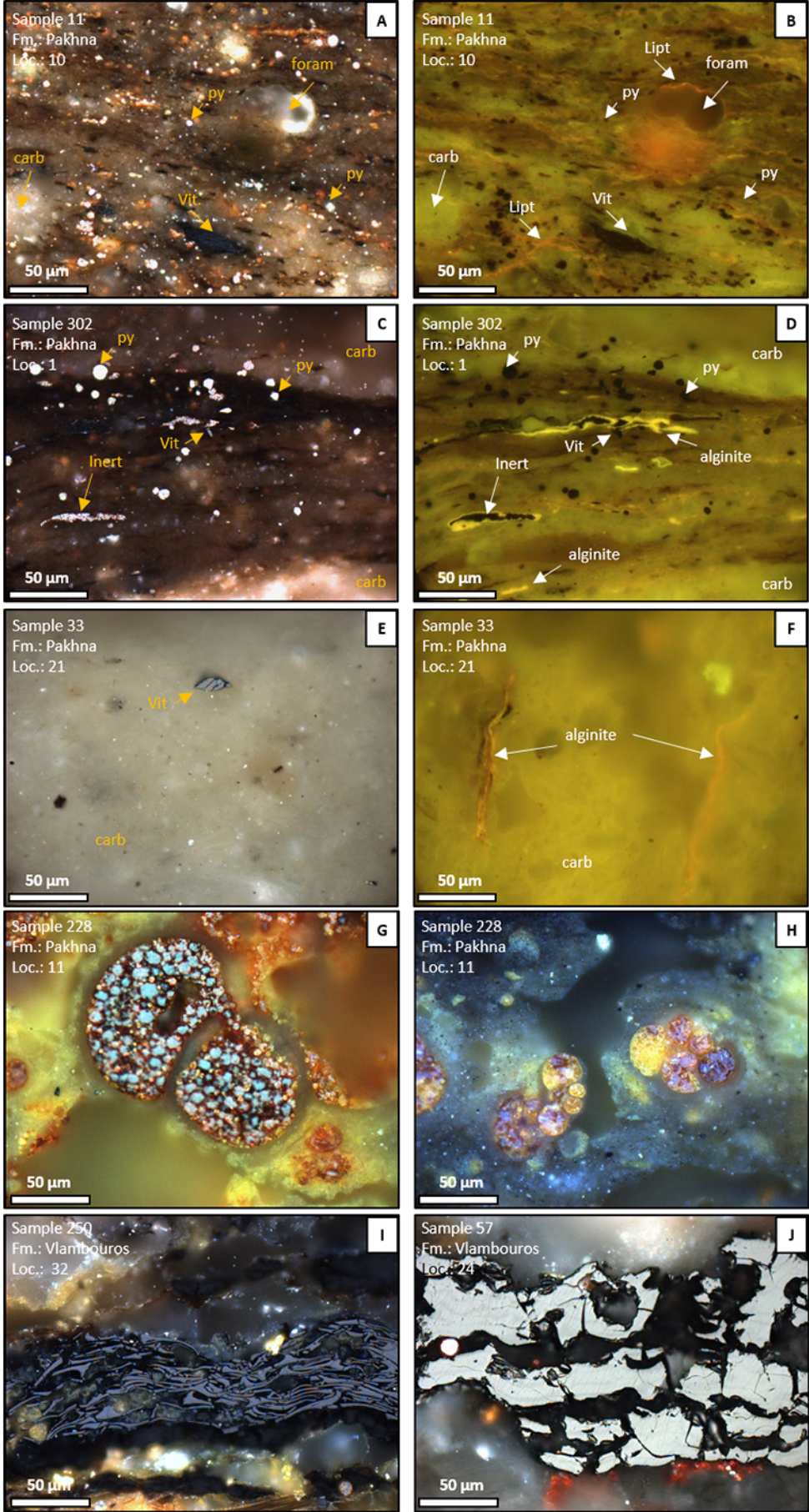
Sample 11
Fm.: Pakhna
Loc.: 10
A
foram
py
carb
py
Vit
50 µm
Sample 11
Fm.: Pakhna
Loc.: 10
B
Lipt
foram
py
carb
py
Lipt
Vit
50 µm
Sample 302
Fm.: Pakhna
Loc.: 1
C
py
carb
py
Vit
Inert
50 µm
carb
Sample 302
Fm.: Pakhna
Loc.: 1
D
py
carb
py
Vit
alginite
Inert
alginite
50 µm
carb
Sample 33
Fm.: Pakhna
Loc.: 21
E
Vit
carb
50 µm
Sample 33
Fm.: Pakhna
Loc.: 21
F
alginite
carb
50 µm
Sample 228
Fm.: Pakhna
Loc.: 11
G
50 µm
Sample 228
Fm.: Pakhna
Loc.: 11
H
50 µm
Sample 250
Fm.: Vlambouros
Loc.: 32
I
50 µm
Sample 57
Fm.: Vlambouros
Loc.: 24
J
50 µm

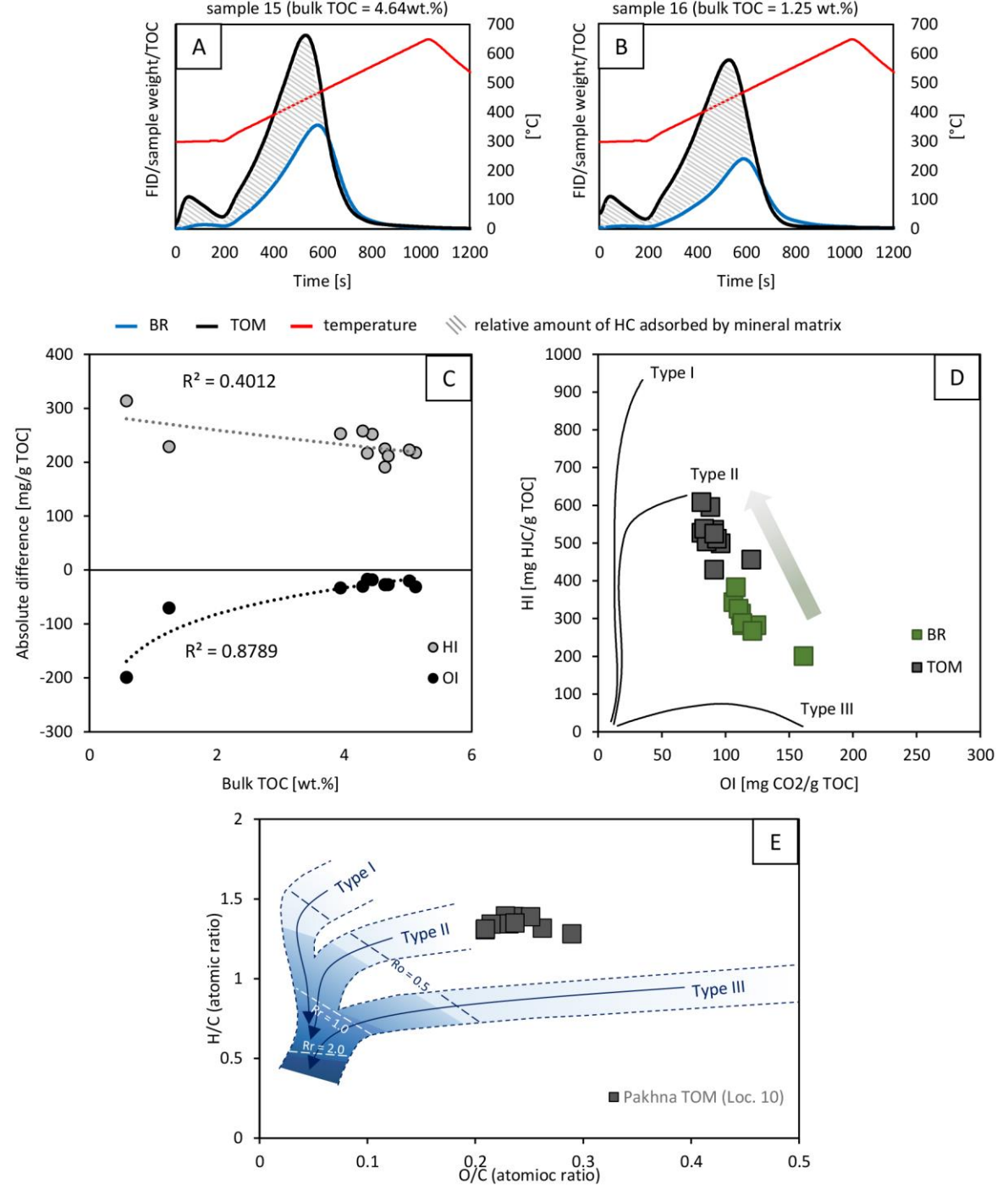
sample 15 (bulk TOC = 4.64wt.%)
A
FID/sample weight/TOC
[°C]
Time [s]
sample 16 (bulk TOC = 1.25 wt.%)
B
BR
TOM
temperature
relative amount of HC adsorbed by mineral matrix
C
R² = 0.4012
R² = 0.8789
HI
OI
Absolute difference [mg/g TOC]
Bulk TOC [wt.%]
D
Type I
Type II
Type III
BR
TOM
HI [mg HJC/g TOC]
OI [mg CO2/g TOC]
E
Type I
Type II
Type III
Ro = 0.5
Rr = 1.0
Rr = 2.0
Pakhna TOM (Loc. 10)
H/C (atomic ratio)
O/C (atomioc ratio)

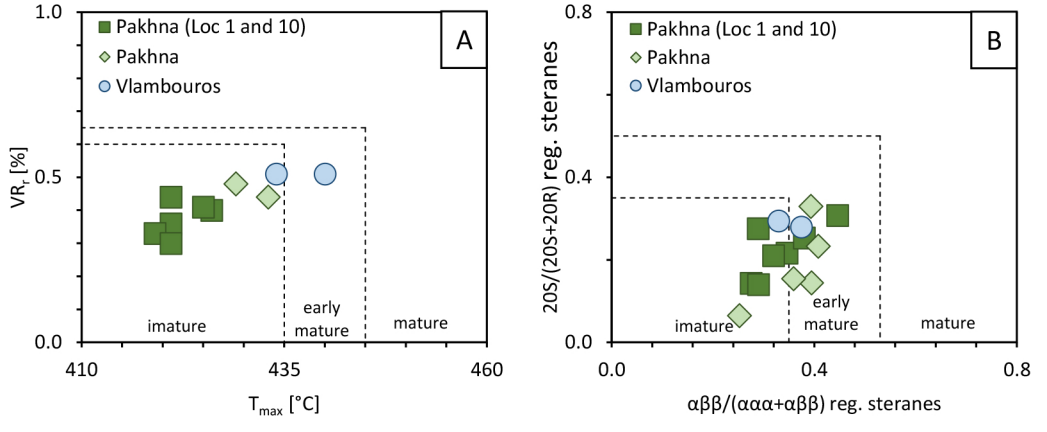
A
Pakhna (Loc 1 and 10)
Pakhna
Vlambouros
VR$_r$ [%]
1.0
0.5
0.0
imature
early mature
mature
410
435
460
T$_{max}$ [°C]
B
Pakhna (Loc 1 and 10)
Pakhna
Vlambouros
20S/(20S+20R) reg. steranes
0.8
0.4
0.0
imature
early mature
mature
0.0
0.4
0.8
αββ/(ααα+αββ) reg. steranes

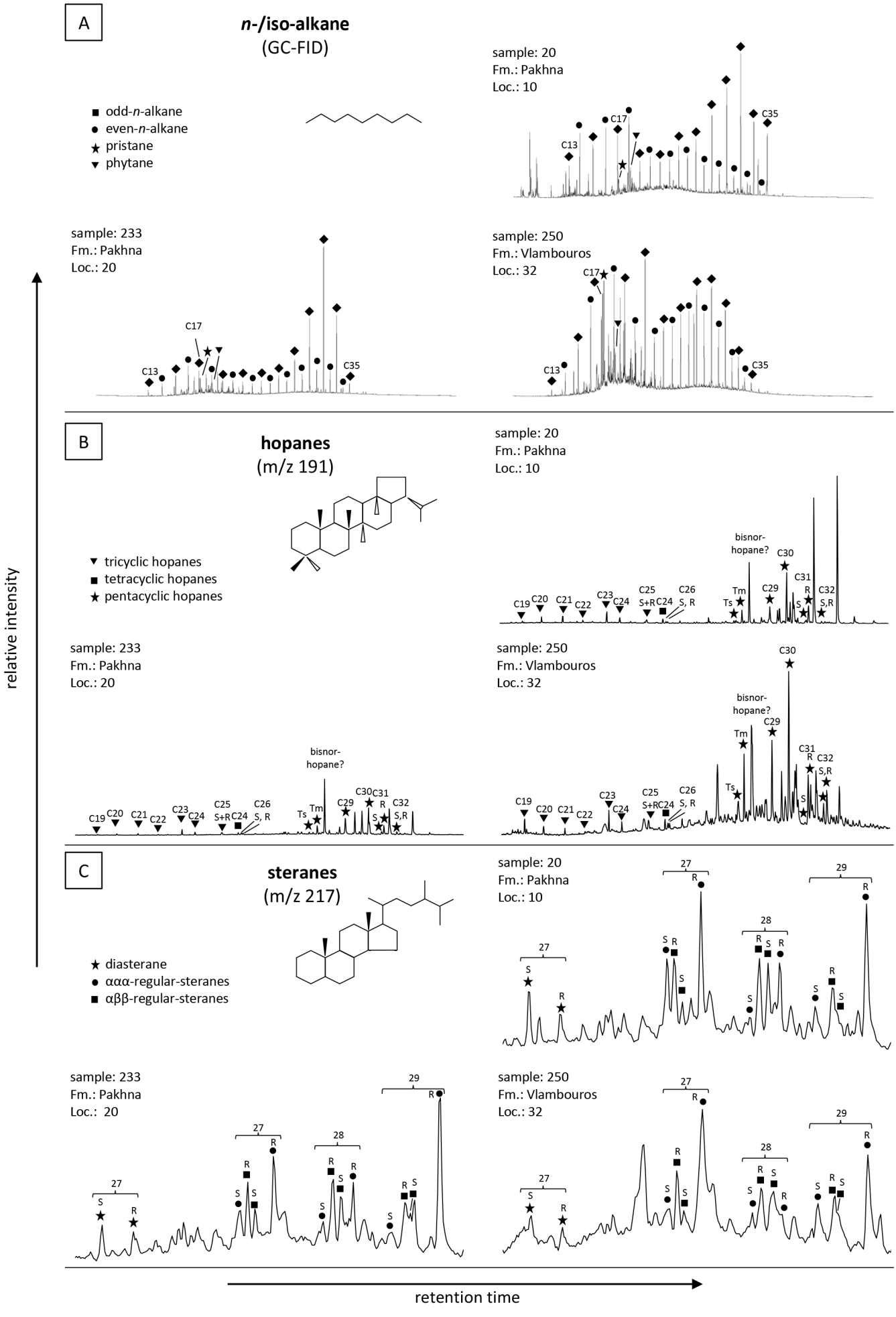
A
n-/iso-alkane
(GC-FID)
odd-n-alkane
even-n-alkane
pristane
phytane
sample: 20
Fm.: Pakhna
Loc.: 10
C13
C17
C35
sample: 233
Fm.: Pakhna
Loc.: 20
sample: 250
Fm.: Vlambouros
Loc.: 32
B
hopanes
(m/z 191)
tricyclic hopanes
tetracyclic hopanes
pentacyclic hopanes
bisnor-hopane?
C19
C20
C21
C22
C23
C24
C25 S+R
C26 S, R
Ts
Tm
C29
C30
C31 R
C32 S,R
C
steranes
(m/z 217)
diasterane
ααα-regular-steranes
αββ-regular-steranes
27
28
29
S
R
relative intensity
retention time

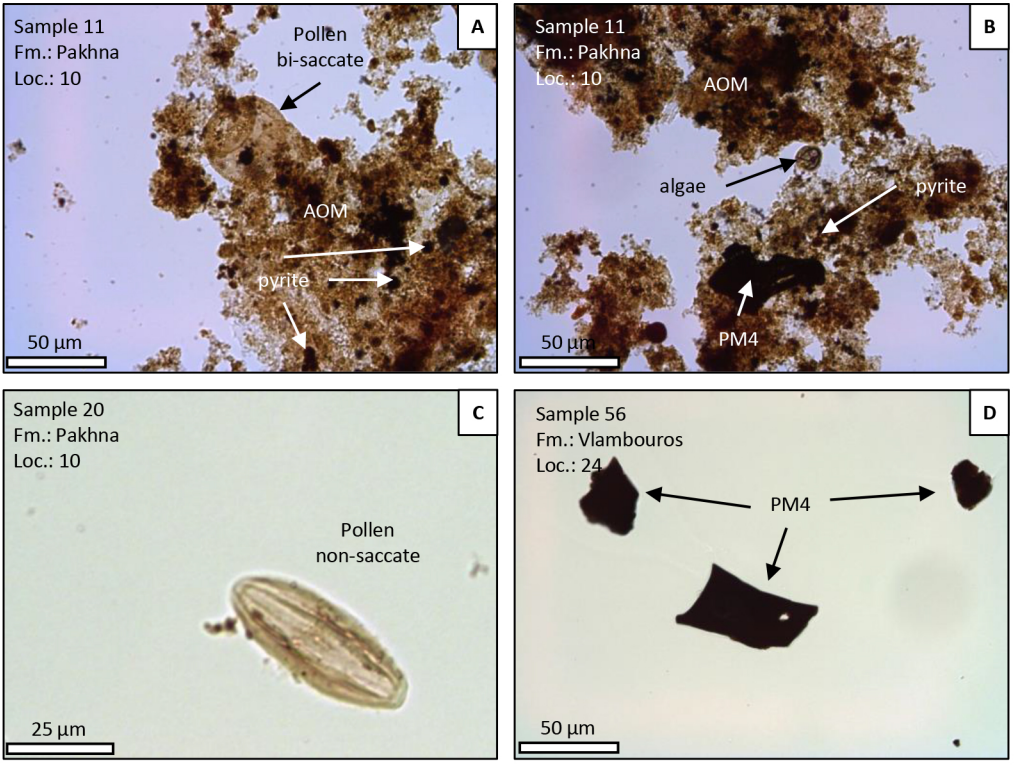
Sample 11
Fm.: Pakhna
Loc.: 10
A
Pollen
bi-saccate
AOM
pyrite
50 µm
Sample 11
Fm.: Pakhna
Loc.: 10
B
AOM
algae
pyrite
PM4
50 µm
Sample 20
Fm.: Pakhna
Loc.: 10
C
Pollen
non-saccate
25 µm
Sample 56
Fm.: Vlambouros
Loc.: 24
D
PM4
50 µm

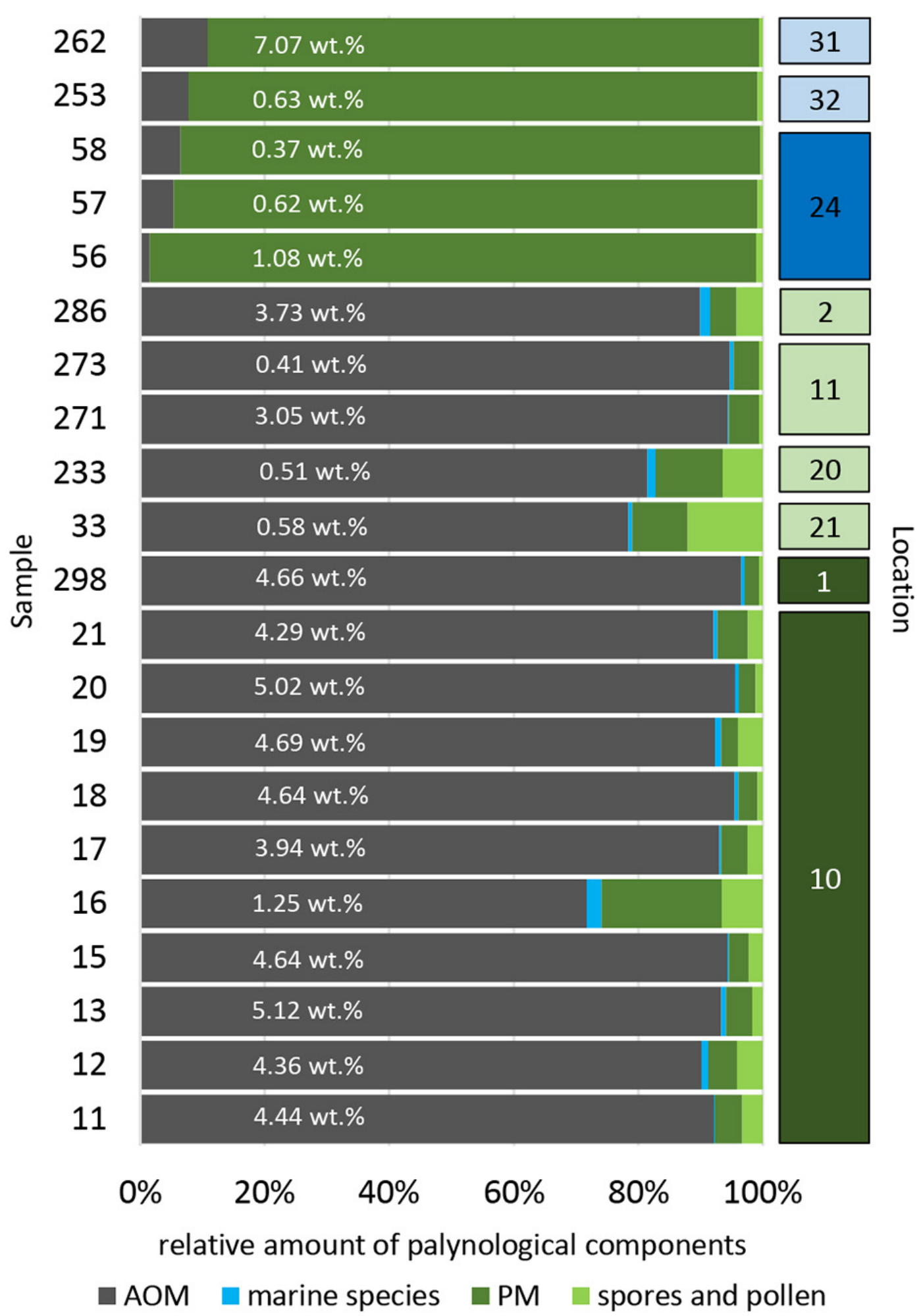
Sample
Location
262
253
58
57
56
286
273
271
233
33
298
21
20
19
18
17
16
15
13
12
11
7.07 wt.%
0.63 wt.%
0.37 wt.%
0.62 wt.%
1.08 wt.%
3.73 wt.%
0.41 wt.%
3.05 wt.%
0.51 wt.%
0.58 wt.%
4.66 wt.%
4.29 wt.%
5.02 wt.%
4.69 wt.%
4.64 wt.%
3.94 wt.%
1.25 wt.%
4.64 wt.%
5.12 wt.%
4.36 wt.%
4.44 wt.%
31
32
24
2
11
20
21
1
10
0%
20%
40%
60%
80%
100%
relative amount of palynological components
AOM
marine species
PM
spores and pollen

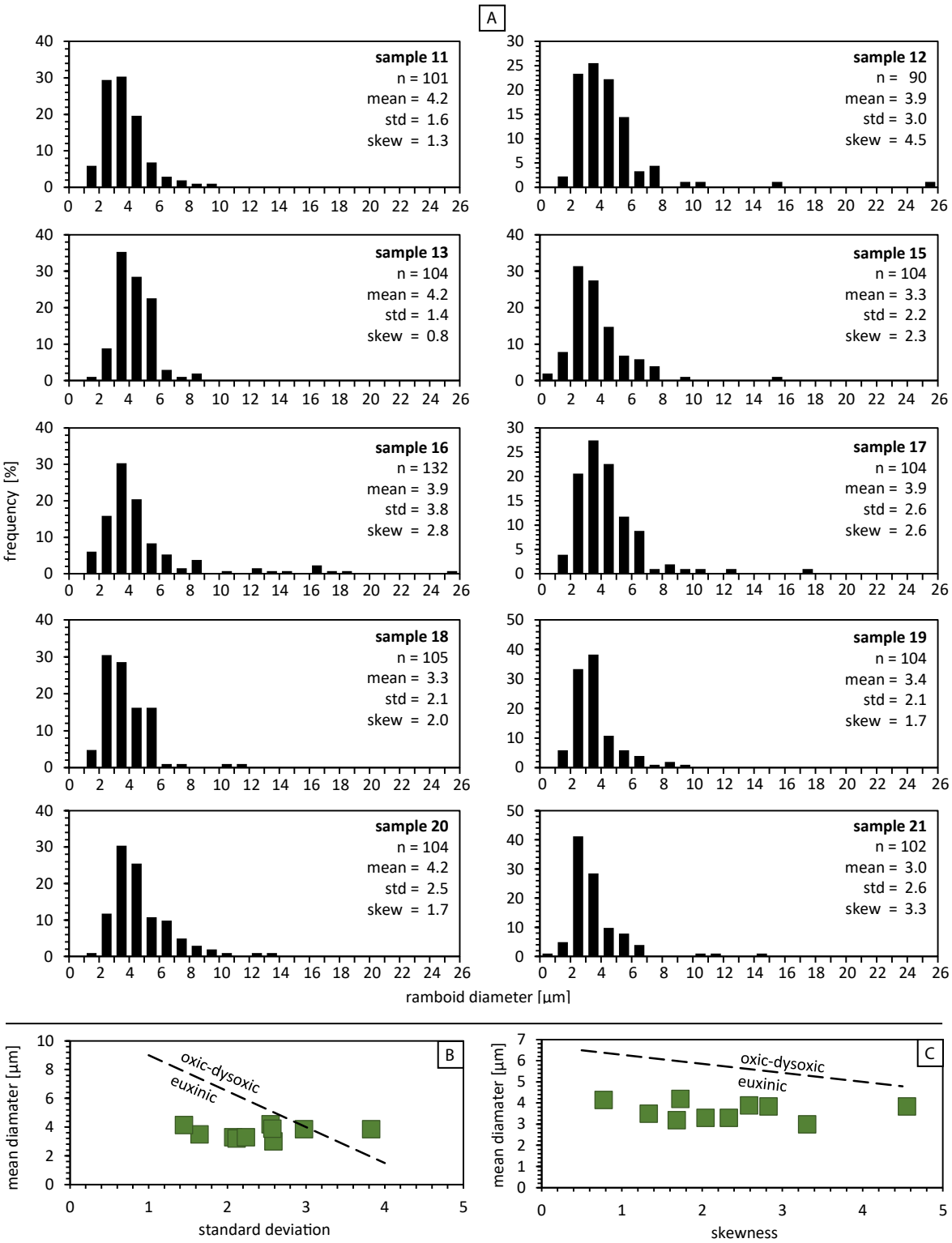
A
sample 11
n = 101
mean = 4.2
std = 1.6
skew = 1.3
sample 12
n = 90
mean = 3.9
std = 3.0
skew = 4.5
sample 13
n = 104
mean = 4.2
std = 1.4
skew = 0.8
sample 15
n = 104
mean = 3.3
std = 2.2
skew = 2.3
sample 16
n = 132
mean = 3.9
std = 3.8
skew = 2.8
sample 17
n = 104
mean = 3.9
std = 2.6
skew = 2.6
sample 18
n = 105
mean = 3.3
std = 2.1
skew = 2.0
sample 19
n = 104
mean = 3.4
std = 2.1
skew = 1.7
sample 20
n = 104
mean = 4.2
std = 2.5
skew = 1.7
sample 21
n = 102
mean = 3.0
std = 2.6
skew = 3.3
frequency [%]
ramboid diameter [µm]
B
oxic-dysoxic
euxinic
mean diamater [µm]
standard deviation
C
oxic-dysoxic
euxinic
mean diamater [µm]
skewness

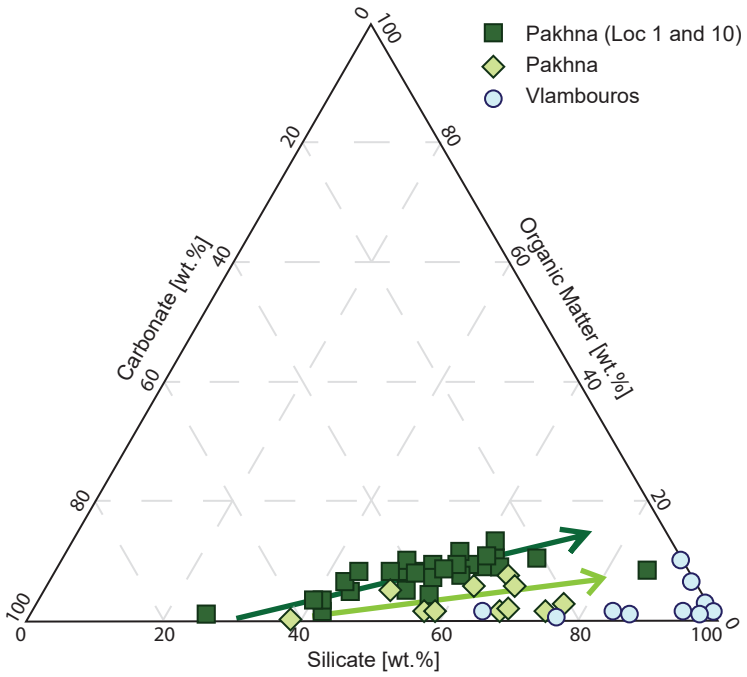
Pakhna (Loc 1 and 10)
Pakhna
Vlambouros
Carbonate [wt.%]
Organic Matter [wt.%]
Silicate [wt.%]
0
20
40
60
80
100

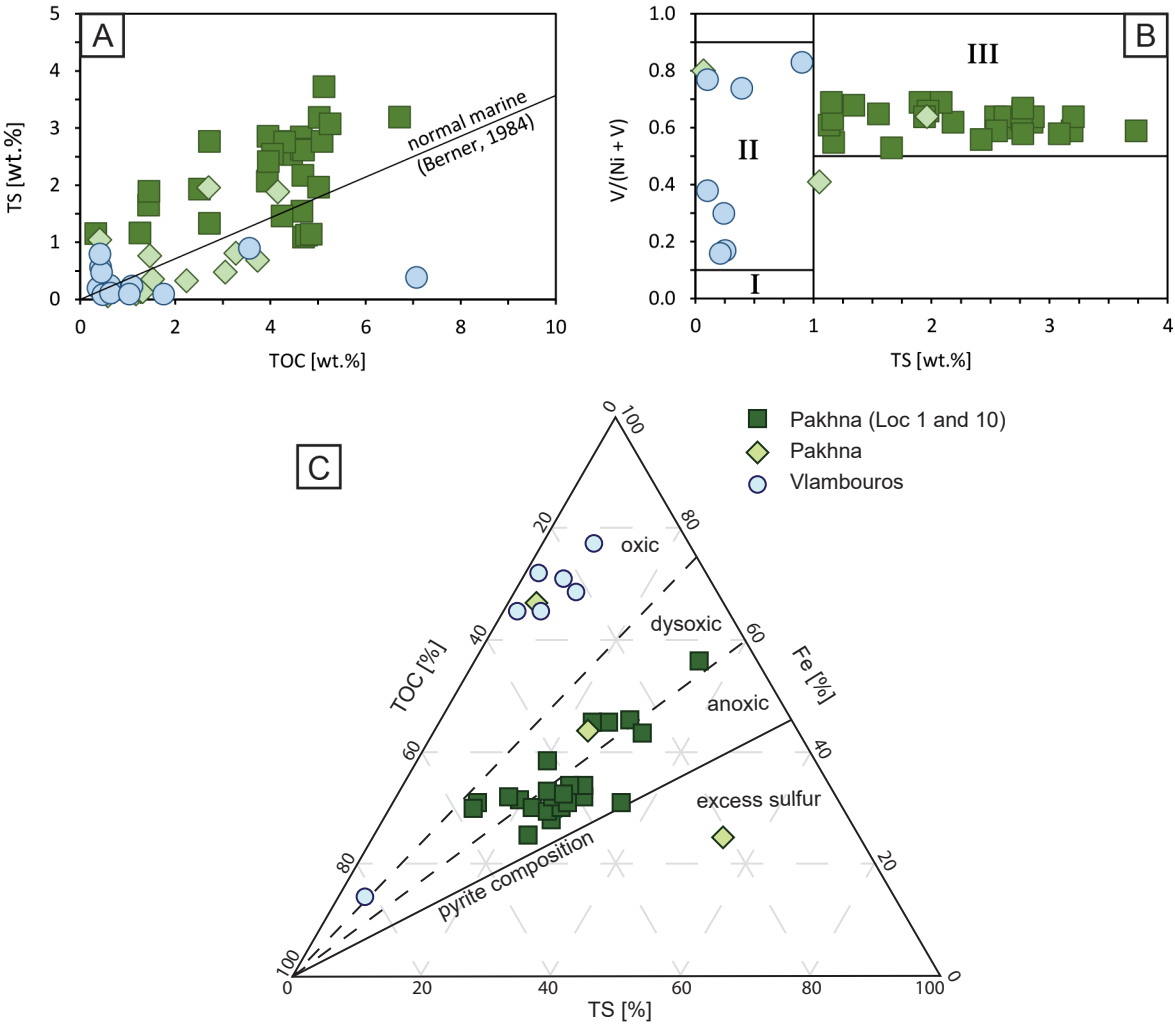
A
TS [wt.%]
TOC [wt.%]
normal marine
(Berner, 1984)
B
V/(Ni + V)
TS [wt.%]
I
II
III
C
Pakhna (Loc 1 and 10)
Pakhna
Vlambouros
oxic
dysoxic
anoxic
excess sulfur
pyrite composition
TOC [%]
Fe [%]
TS [%]

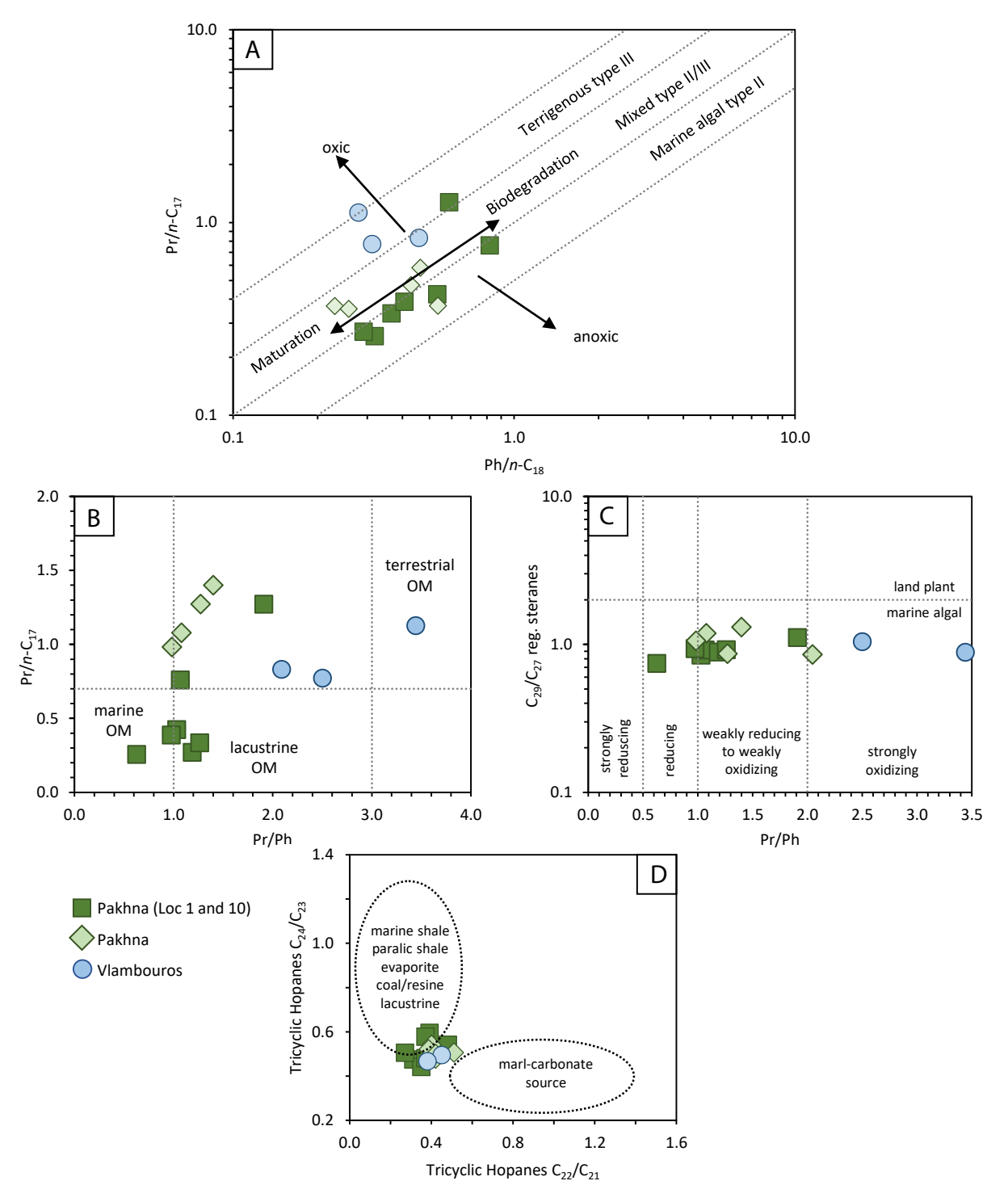
A
10.0
1.0
0.1
0.1
1.0
10.0
Pr/n-C17
Ph/n-C18
oxic
Biodegradation
Maturation
anoxic
Terrigenous type III
Mixed type II/III
Marine algal type II
B
2.0
1.5
1.0
0.5
0.0
0.0
1.0
2.0
3.0
4.0
Pr/n-C17
Pr/Ph
terrestrial OM
marine OM
lacustrine OM
C
10.0
1.0
0.1
0.0
0.5
1.0
1.5
2.0
2.5
3.0
3.5
C29/C27 reg. steranes
Pr/Ph
land plant
marine algal
strongly reducing
reducing
weakly reducing to weakly oxidizing
strongly oxidizing
Pakhna (Loc 1 and 10)
Pakhna
Vlambouros
D
1.4
1.0
0.6
0.2
0.0
0.4
0.8
1.2
1.6
Tricyclic Hopanes C24/C23
Tricyclic Hopanes C22/C21
marine shale
paralic shale
evaporite
coal/resine
lacustrine
marl-carbonate source

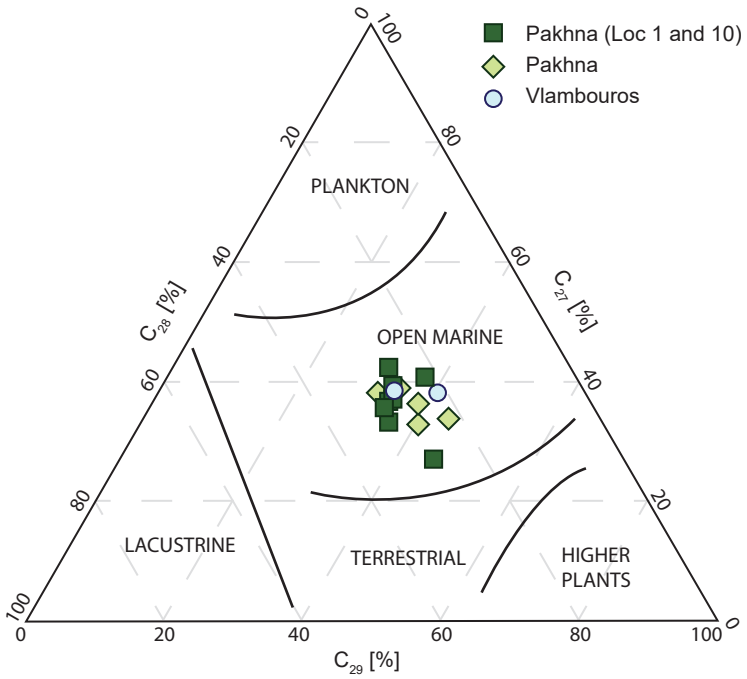
Pakhna (Loc 1 and 10)
Pakhna
Vlambouros
PLANKTON
OPEN MARINE
LACUSTRINE
TERRESTRIAL
HIGHER
PLANTS
C28 [%]
C27 [%]
C29 [%]
0
20
40
60
80
100

Loc.	Formation	Age	Latitude	Longitude
1*	Upper Pakhna	Upper Miocene	35°01'58.27"N	33°20'35.56"E
2*	(Upper?) Pakhna	(Upper) Miocene	35°01'57.25"N	33°20'39.12"E
3	Lower Lefkara	Late Cretaceous	34°59'53.20"N	33°25'29.39"E
4	Nicosia	Pliocene	35°00'52.41"N	33°30'36.96"E
5	Upper Pakhna	Upper Miocene	35°00'23.91"N	33°30'25.53"E
6	Lower Lefkara	Late Cretaceous	35°00'50.45"N	33°33'24.35"E
7	Lower Lefkara	Late Cretaceous	35°01'47.35"N	33°35'42.05"E
8	Lower Lefkara	Late Cretaceous	35°02'02.35"N	33°35'58.67"E
9	Lower Lefkara	Late Cretaceous	34°59'47.69"N	33°36'51.27"E
10*	Upper Pakhna	Upper Miocene	34°57'29.54"N	33°34'43.13"E
11*	Pakhna	Miocene	34°48'08.56"N	33°26'08.74"E
12*	Pakhna	Miocene	34°46'38.21"N	33°23'56.29"E
13	Pakhna	Miocene	34°50'13.50"N	33°23'58.10"E
14	Pakhna	Miocene	34°49'40.04"N	33°23'29.82"E
15	Pakhna	Miocene	34°49'04.70"N	33°23'37.92"E
16	(Upper?) Pakhna	(Upper) Miocene	34°45'53.18"N	33°18'03.91' E
17	Moni Melange	Triassic to Cretaceous	34°45'14.58"N	33°06'23.90"E
18	Pakhna	Miocene	34°45'51.40"N	32°55'52.38"E
19	Pakhna	Miocene	34°45'43.12"N	32°50'35.95"E
20*	Pakhna	Miocene	34°46'25.23"N	32°49'55.88"E
21*	(Upper?) Pakhna	(Upper) Miocene	34°48'55.58"N	32°49'27.02"E
22	Lower Lefkara	Late Cretaceous	34°51'22.39"N	32°52'16.77"E
23	Pakhna	Miocene	34°39'37.84"N	32°39'08.18"E
24*	Vlambouros	Middle Triassic	34°47'39.67"N	32°39'22.08"E
25	Episkopi	Middle Jurassic	34°48'12.56"N	32°38'43.71"E
26	Vlambouros	Middle Triassic	34°44' 05.05"N	32°35' 54.18"E
27	Episkopi	Middle Jurassic	34°52' 08.85"N	32°36'25.95"E
28	Episkopi	Middle Jurassic	34°51'58.19"N	32°36'10.41"E
29	Episkopi	Middle Jurassic	34°52'29.37"N	32°35'48.04"E
30	Episkopi	Middle Jurassic	34°52'34.04"N	32°35'38.65"E
31*	Vlambouros	Middle Triassic	34°58'54.70"N	32°19'09.44"E
32*	Vlambouros	Middle Triassic	34°58'50.01"N	32°19'00.37"E

Sample	Loc.	Fm.	TOC [wt.%]	TIC [wt.%]	S1 [mg HC/g rock]	S2 [mg HC/g rock]	S3 [mg CO_2/g rock]	HI [mg HC/g TOC]	OI [mg CO_2/g TOC]	T_{max} [°C]
11	10	P	4.44	4.91	0.28	15.26	4.69	344	106	421
12	10	P	4.36	3.2	0.22	12.33	4.92	283	113	419
13	10	P	5.12	3.77	0.29	15.85	5.72	310	112	421
15	10	P	4.64	4.27	0.32	17.82	5.01	384	108	424
16	10	P	1.25	6.65	0.04	2.51	2.01	201	161	426
17	10	P	3.94	4.58	0.2	11.16	4.87	283	124	421
18	10	P	4.64	4.79	0.25	14.55	5.18	314	112	419
19	10	P	4.69	4.34	0.25	15.34	5.15	327	110	426
20	10	P	5.02	3.34	0.22	14.52	5.65	289	113	421
21	10	P	4.29	3.43	0.17	11.51	5.17	268	121	423
33	21	P	0.58	7.29	0.01	0.6	1.34	143	319	429
227	12	P	3.66	6.07	0.14	11.80	2.75	322	75	429
228	11	P	1.57	1.03	0.06	2.33	1.93	148	123	434
233	20	P	0.51	4.93	0.04	0.50	1.05	97	206	433
271	11	P	3.05	5.22	0.10	7.05	1.80	231	59	434
272	11	P	2.23	6.68	0.10	6.45	1.34	289	60	433
273	11	P	0.41	8.75	0.04	0.27	0.69	65	166	434
274	10	P	4.69	4.45	0.20	10.81	2.55	230	54	420
275	10	P	1.43	4.63	0.08	2.57	0.98	180	69	---
276	10	P	4.75	5.69	0.21	11.48	3.50	241	74	414
277	10	P	5.08	3.19	0.27	11.35	3.20	224	63	420
279	10	P	4.04	5.11	0.19	10.23	2.87	253	71	421
280	10	P	1.44	4.79	0.09	3.09	1.06	214	73	425
281	10	P	4.68	3.97	0.20	12.78	3.22	273	69	423
282	10	P	0.32	6.74	0.05	0.20	0.63	63	193	---
283	10	P	6.71	3.01	0.31	22.71	2.34	338	35	420
285	10	P	5.25	2.44	0.19	12.63	2.23	241	42	420
286	2	P	3.73	3.16	0.16	5.81	2.88	156	77	428
287	2	P	1.17	2.77	0.07	0.30	3.34	26	285	---
288	2	P	1.27	4.74	0.08	0.32	3.21	25	252	---
289	2	P	1.31	2.56	0.09	0.28	3.86	21	295	---
290	2	P	1.06	4.95	0.08	0.30	1.87	29	176	---
291	2	P	0.71	3.61	0.06	0.25	2.10	36	297	---
292	2	P	1.52	3.43	0.09	1.80	1.50	119	99	427
293	2	P	4.15	3.14	0.17	9.14	2.93	220	70	421
294	2	P	2.70	3.89	0.14	7.00	2.00	259	74	424
295	2	P	3.27	5.25	0.21	5.87	3.38	179	103	427
296	2	P	1.46	2.51	0.09	1.23	2.51	84	171	428
297	1	P	0.31	0.71	0.12	0.27	0.88	88	286	---
298	1	P	4.66	4.20	0.21	11.97	2.52	257	54	424
299	1	P	3.93	4.40	0.16	8.70	2.13	221	54	423
300	1	P	4.85	4.81	0.19	11.14	2.30	230	47	422
301	1	P	4.24	3.93	0.17	9.68	2.18	228	51	422
302	1	P	5.01	3.72	0.19	10.81	2.33	216	47	421
303	1	P	2.50	4.99	0.10	3.62	1.70	144	68	428
304	1	P	3.95	4.66	0.08	2.22	1.79	56	45	424
305	1	P	2.71	5.97	0.18	7.46	2.26	276	83	427
306	1	P	2.71	5.97	0.12	4.27	2.08	158	77	425
56	24	V	1.08	1.66	0.00	0.50	0.98	41	81	440
57	24	V	0.62	4.01	0.00	0.26	0.8	40	123	442
58	24	V	0.37	2.73	0.00	0.12	0.54	33	150	441
250	32	V	3.55	0.02	0.03	0.65	1.91	18	54	---
251	32	V	1.75	0.02	0.03	1.00	0.72	57	41	---
252	32	V	0.47	1.48	0.03	0.30	0.43	62	91	---
253	32	V	0.63	0.54	0.03	0.33	0.38	52	61	---
254	31	V	0.42	0.02	0.03	0.18	0.56	43	134	---
260	31	V	1.03	0.18	0.04	0.60	0.22	59	21	437
261	31	V	0.44	0.01	0.03	0.32	0.09	73	21	---
262	31	V	7.07	0.03	0.06	2.12	2.69	30	38	434
264	31	V	0.41	0.02	0.00	0.50	0.98	86	48	---

Sample	Bulk rock				Total organic matter			
	TOC [wt.%]	HI [mg HC/g rock]	OI [mg CO_2/g rock]	T_{max} [°C]	TOC [wt.%]	HI [mg HC/g rock]	OI [mg CO_2/g rock]	T_{max} [°C]
11	4.44	344	106	421	57.26	596	88	406
12	4.36	283	113	419	49.66	500	96	398
13	5.12	310	112	421	50.07	528	81	404
15	4.64	384	108	424	50.67	609	81	406
16	1.25	201	161	426	31.48	430	91	405
17	3.94	283	124	421	49.91	536	91	402
18	4.64	314	112	419	48.08	505	85	398
19	4.69	327	110	426	53.97	539	83	401
20	5.02	289	113	421	49.49	512	93	397
21	4.29	268	121	423	50.78	526	91	401
33	0.58	143	319	429	46.69	457	120	414

Fm.	Loc.	samples	VRr	$n_{samples}$	n_{total}	Std dev
P	1	302, 306	0.43	2	85	0.08
P	10	11, 12, 13, 15, 16, 17, 18, 19, 20, 21	0.33	10	479	0.05
P	11	228, 271	0.44	2	41	0.07
P	21	33	0.48	1	57	0.07
V	24	56, 57, 58	0.51	3	148	0.07
V	31	262	0.51	1	97	0.03
V	32	250, 251	0.63	2	165	0.06

Sample	Loc.	Fm.	Pr/Ph[a]	Pr/*n*-C_{17}	Ph/*n*-C_{18}	TAR[b]	CPI[c]	OEP[d]
17	10	P	1.91	1.27	0.59	8.57	2.56	1.59
18	10	P	1.03	0.43	0.53	3.01	3.35	1.84
19	10	P	1.07	0.76	0.82	10.29	3.08	1.91
20	10	P	0.63	0.26	0.32	3.98	2.53	1.43
33	21	P	1.08	0.37	0.54	4.98	2.23	1.22
233	20	P	1.40	0.37	0.23	8.59	2.34	1.17
272	11	P	0.98	0.47	0.43	2.72	2.56	1.25
286	2	P	1.27	0.36	0.26	3.82	3.08	1.49
296	2	P	2.05	0.58	0.46	6.72	4.39	1.45
297	1	P	1.19	0.27	0.29	1.25	1.78	0.43
302	1	P	1.26	0.34	0.37	0.66	2.91	2.08
306	1	P	0.98	0.39	0.41	7.40	3.35	1.29
56	24	V	2.09	0.83	0.46	1.44	0.49	0.95
250	32	V	3.44	1.13	0.28	0.04	0.43	0.10
262	31	V	2.50	0.77	0.31	0.51	0.93	1.26

[a]pristane/phytane, [b]Terrigenous Aquatic Ratio = (n-C_{27} + n-C_{29} + n-C_{31})/(n-C_{15} + n-C_{17} + n-C_{19})
[c]Carbon Preference Index = ((2 * (n-C_{23} + n-C_{25} + n-C_{27} + n-C_{29}))/(n-C_{22} + 2 * (n-C_{24} + n-C_{26} + n-C_{28}) + n-C_{30})
[d]Odd Even Predominance = (n-C_{21} + 6 * n-C_{23} + n-C_{25})/(4 * n-C_{22} + 4 * n-C_{24})

Sample	Loc.	Fm.	Regular steranes					Hopanes					
			C_{27} [%]	C_{28} [%]	C_{29} [%]	20S/(20S+20R)	αββ/(ααα+αββ)	Ts/(Ts+Tm)	GI*	C_{22}/C_{21}	C_{24}/C_{23}	C_{26}/C_{25} tricyclic	C_{29}/C_{30}
17	10	P	33	31	36	0.22	0.35	0.28	0.27	0.39	0.60	0.52	0.46
18	10	P	39	27	33	0.28	0.29	0.18	0.55	0.31	0.48	0.65	0.44
19	10	P	37	28	34	0.14	0.28	0.12	0.23	0.37	0.58	0.94	0.41
20	10	P	42	26	31	0.21	0.32	0.17	0.04	0.35	0.44	0.64	0.34
33	21	P	33	27	40	0.14	0.39	0.20	0.72	0.40	0.54	0.76	0.41
233	20	P	34	22	44	0.15	0.36	0.29	0.40	0.51	0.51	0.62	0.02
272	11	P	37	25	39	0.06	0.25	0.06	0.37	0.42	0.48	0.82	0.44
286	2	P	39	27	34	0.23	0.41	0.24	0.33	0.39	0.52	0.80	0.47
296	2	P	38	30	32	0.33	0.39	0.25	0.78	0.42	0.50	0.80	0.54
297	1	P	41	22	37	0.25	0.38	0.31	0.88	0.37	0.48	0.82	0.91
302	1	P	37	29	34	0.14	0.29	0.20	0.49	0.27	0.51	0.91	0.43
306	1	P	36	31	34	0.31	0.45	0.25	0.54	0.48	0.54	0.73	0.37
56	24	V	---	---	---	---	---	---	---	---	---	---	---
250	32	V	39	27	34	0.30	0.33	0.14	1.42	0.45	0.50	0.74	0.48
262	31	V	38	21	40	0.28	0.37	0.19	0.28	0.38	0.47	0.77	0.00

*Gammacerane Index = (10 x gammacerane)/C30 hopane)

Sample	Loc.	Fm.	TS [wt.%]	Fe [wt.%]	Ni [ppm]	V [ppm]
11	10	P	2.54	2.67	128	225
12	10	P	2.77	3.73	163	315
13	10	P	3.73	4.15	164	235
15	10	P	2.85	3.28	152	244
16	10	P	1.17	2.00	101	122
17	10	P	2.86	3.48	138	245
18	10	P	2.64	3.14	140	213
19	10	P	2.62	3.43	139	245
20	10	P	3.19	3.93	172	246
21	10	P	2.76	3.39	135	233
33	21	P	0.07	1.33	90	367
271	11	P	0.48	---	---	---
272	11	P	0.33	---	---	---
273	11	P	1.05	0.49	45	31
274	10	P	1.10	---	---	---
275	10	P	1.66	2.65	89	101
276	10	P	1.13	2.52	107	166
277	10	P	2.77	3.31	148	204
279	10	P	2.55	2.99	125	179
280	10	P	1.9	2.55	74	167
281	10	P	2.18	2.93	125	207
282	10	P	1.16	1.91	49	85
283	10	P	3.2	3.3	146	263
285	10	P	3.08	4.07	170	235
286	2	P	0.69	---	---	---
287	2	P	0.10	---	---	---
288	2	P	0.14	---	---	---
289	2	P	0.14	---	---	---
290	2	P	0.19	---	---	---
291	2	P	0.14	---	---	---
292	2	P	0.36	---	---	---
293	2	P	1.89	---	---	---
294	2	P	1.96	3.62	157	283
295	2	P	0.81	---	---	---
296	2	P	0.77	---	---	---
297	1	P	6.20	---	---	---
298	1	P	1.55	2.98	175	325
299	1	P	2.08	2.91	120	272
300	1	P	1.15	2.71	127	280
301	1	P	1.47	---	---	---
302	1	P	1.97	3.16	144	285
303	1	P	1.94	3.56	128	231
304	1	P	2.42	2.88	119	152
305	1	P	2.77	2.49	116	240
306	1	P	1.34	2.52	94	202
56	24	V	0.24	2.50	162	70
57	24	V	0.25	1.95	325	66
58	24	V	0.21	1.94	326	62
250	33	V	0.90	11.05	32	160
251	33	V	0.10	3.52	184	114
252	33	V	0.09	---	---	---
253	33	V	0.12	---	---	---
254	32	V	0.57	---	---	---
260	32	V	0.10	2.89	44	149
261	32	V	0.48	---	---	---
262	32	V	0.39	1.21	51	145
264	32	V	0.80	---	---	---